

# 3D bioprinted multi-layered cell constructs with gradient core-shell interface for tendon-to-bone tissue regeneration

WonJin Kim<sup>a,1</sup>, Dong Rak Kwon<sup>b,1</sup>, Hyeongjin Lee<sup>c,1</sup>, JaeYoon Lee<sup>a</sup>, Yong Suk Moon<sup>d</sup>, Sang Chul Lee<sup>e,\*\*</sup>, Geun Hyung Kim<sup>a,f,g,\*</sup>

<sup>a</sup> Department of Precision Medicine, Sungkyunkwan University School of Medicine (SKKU-SOM), Suwon, 16419, Republic of Korea

<sup>b</sup> Department of Rehabilitation Medicine, School of Medicine, Catholic University of Daegu, Daegu, Republic of Korea

<sup>c</sup> Department of Biotechnology and Bioinformatics, Korea University, Sejong, Republic of Korea

<sup>d</sup> Department of Anatomy, School of Medicine, Catholic University of Daegu, Daegu, Republic of Korea

<sup>e</sup> Department and Research Institute of Rehabilitation Medicine, Yonsei University, College of Medicine, 50-1 Yonsei-ro, Seodaemun-gu, Seoul, 03722, Republic of Korea

<sup>f</sup> Institute of Quantum Biophysics, Department of Biophysics, Sungkyunkwan University, Suwon, Gyeonggi-do, 16419, Republic of Korea

<sup>g</sup> Biomedical Institute for Convergence at SKKU (BICS), Sungkyunkwan University, Suwon, 16419, Republic of Korea

## ARTICLE INFO

### Keywords:

Bioprinting  
Complex cell-construct  
Tendon-bone interface  
Tissue engineering

## ABSTRACT

Rotator cuff tears are common among physically active individuals and often require surgical intervention owing to their limited self-healing capacity. This study proposes a new bioprinting approach using bone- and tendon tissue-specific bioinks derived from decellularized extracellular matrix, supplemented with hydroxyapatite and TGF- $\beta$ /poly(vinyl alcohol) to fabricate engineered tendon-to-bone complex tissue. To achieve this goal, a core-shell nozzle system attached to a bioprinter enables the effective and simultaneous fabrication of aligned tendon tissue, a gradient tendon-bone interface (TBI), and a mechanically improved bone region, mimicking the native tendon-to-bone structure. *In vitro* evaluation demonstrated the well-directed differentiation of human adipose stem cells towards osteogenic and tenogenic lineages in the bone and tendon constructs. In the graded TBI structure, further facilitated fibrocartilage formation and enhanced the integration of tendon-to-bone tissues compared to non-graded structures *in vitro*. Furthermore, using a rabbit rotator cuff tear model, implantation of the biologically graded constructs significantly promoted the rapid regeneration of full-thickness tendon-to-bone tissue, including the formation of a high-quality TBI *in vivo*. This bioprinting approach not only improved mechanical properties and tissue integration but also enhanced angiogenesis and extracellular matrix (ECM) formation, demonstrating its potential as a promising platform for the regeneration of tendon-to-bone complex tissues.

## 1. Introduction

The tendon-bone interface (TBI), a crucial junction composed of tendons, transitional fibrocartilage, and bone, relieves stress concentration and optimizes the transmission of external loads within the body [1–4]. The TBI, found in diverse regions in the human body between two different tissues including bone-tendon and bone-ligament, involves complex hierarchical tissue structures encompassing gradient mineral distribution and various cell phenotypes for efficient load transfer, transitioning from uncalcified to calcified fibrocartilage at the interface

region near the tendon and bone tissues, respectively [1–4]. Tendons possess high tensile strength, while the bone is optimized for compressive loading, with the intermediate regions bridging the gap between their differing mechanical properties [5]. This progressive change is essential for minimizing stress concentrations between the tendon and bone.

Rotator cuff tears (RCTs) are prevalent among athletic and physically active individuals, and often necessitate surgical reconstruction for healing. However, despite being widely used, because of the intricate biological composition and limited self-healing capacity of TBI, even

Peer review under responsibility of KeAi Communications Co., Ltd.

\* Corresponding author. Department of Precision Medicine, Sungkyunkwan University School of Medicine (SKKU-SOM), Suwon, 16419, Republic of Korea.

\*\* Corresponding author.

E-mail addresses: [bettertomo@yuhs.ac](mailto:bettertomo@yuhs.ac) (S.C. Lee), [gkimbme@skku.edu](mailto:gkimbme@skku.edu) (G.H. Kim).

<sup>1</sup> These authors contributed equally to this work.

<https://doi.org/10.1016/j.bioactmat.2024.10.002>

Received 18 July 2024; Received in revised form 12 September 2024; Accepted 1 October 2024

Available online 11 October 2024

2452-199X/© 2024 The Authors. Publishing services by Elsevier B.V. on behalf of KeAi Communications Co. Ltd. This is an open access article under the CC BY-NC-ND license (<http://creativecommons.org/licenses/by-nc-nd/4.0/>).

successful surgical interventions can result in the formation of disorganized fibrovascular scar tissue and inadequate mechanical strength transmission [6–8]. Previous studies examining the tendon-to-bone healing process following tendon reattachment surgery also found that the interface between the tendon and bone remained hypercellular, with no fibrocartilage layer observed [9,10]. This phenomenon, including re-tearing, emphasizes the necessity for more effective strategies for TBI regeneration.

Tissue engineering technology has emerged as a promising alternative that uses synthetic or natural biomaterials, stem cells, and bioactive molecules to enhance TBI healing [11–14]. While biomimetic stratified or multi-layered scaffolds have shown high potential healing capabilities, achieving a functional TBI with a biologically graded structure from bone to tendon remains a significant challenge [11–14].

Recently, biomimetic strategies utilizing multicellular structures and bioprinting processes using unique cell-specific bioinks have been explored to regenerate complex musculoskeletal tissues [15,16]. However, fabricating precisely controlled biological and biomechanical engineered cell constructs for obtaining successful regenerated fibrocartilage and enthesis is still challenging owing to insufficient biological complexity, inadequate vascularization, low sustainability for external mechanical forces, and insufficient biostructural formation at the TBI [3, 11–14].

The design of cell-laden bioinks tailored for bioprinting is important for the regeneration of biomimetic TBI regeneration [14,17,18]. Ideal bioinks mimic tissue microenvironments and modulate multiple cell activities to achieve the desired biological functions. In particular, decellularized extracellular matrix (dECM)-based bioinks have demonstrated superior regulation and promotion of tissue-specific cell proliferation and differentiation compared to single-component bioinks, such as collagen and hyaluronic acid [19,20]. Although dECM-based bioinks can provide outstanding regeneration of the TBI because of several tissue-specific biomolecules, dECM-based bioinks still have shortcomings, such as poor mechanical properties in the bone region and low rheological properties that can promote uniaxial topographical cues in the tendon region [21,22]. Furthermore, the efficient differentiation of various stem cells and insufficient biological components (bioceramic and growth factors) within the bone-tendon engineering structure present challenges.

In particular, various strategies for designing the TBI region have been proposed to achieve successful regeneration of RCTs [23]. Two typical methods for fabricating the TBI region are generally used: (1) direct attachment of the bone and tendon regions using specific cell-laden biomaterials and (2) gradient distribution from bone to tendon (or vice versa) by manipulating each biological composition [11, 12,24–27]. The first method involves the arbitrary formation of the TBI region by directly attaching each cell-laden structure (bone and tendon), whereas the second method involves obtaining multi-layered scaffolds that can systematically induce the TBI region by spatially positioning a mixture of biomaterials from both bone and tendon regions. As expected, the gradient TBI structures more precisely reproduced the hierarchical shape of the TBI region, multiple distributions of cells, and biological components of the TBI tissues compared to directly attached bone and tendon structures.

Although the gradient strategy for TBI regeneration has shown meaningful biological results, a precisely controlled method for fabricating the TBI region is still required. This is because the fabricated TBI region exhibits poor stability at the interface between the tendon and bone tissue. Furthermore, additional mold frames made from synthetic polymers, such as polycaprolactone and non-biodegradable thermoplastic polyurethane, which can induce inflammation, are required to sustain the printed bioinks [14].

Therefore, a new strategy for obtaining a cell-laden structure with a highly efficient gradient and pore structure in the TBI region without using any synthetic polymers or discrete separations at the interfaces is necessary. Additionally, to efficiently achieve a bone-tendon structure, a

simple and effective printing procedure and printing tools are required.

This paper proposes a new fabrication platform that employs bioprinting to efficiently distribute human adipose stem cells (hASCs) and their biological components for TBI interface regeneration. Human mesenchymal stem cells (hMSCs) are known to be less immunogenic because they have low expression levels of HLA major histocompatibility complex (MHC) class I and lack of MHC class II molecules that induce the immune evasion in the xenogenic transplantation. hASCs, which also known as human adipose-derived MSCs, have been proven to have no immune rejection/response issues, in accordance with previous studies [28–32]. Furthermore, due to their self-renewal and multipotent differentiation abilities, hASCs have been suggested for clinical use in the treatment of rotator cuff tears, either as a standalone therapy or as an adjunct to existing surgical procedures. Specifically, hASCs can differentiate into myocytes, osteoblasts, and tenocytes, while also promoting angiogenesis, enhancing matrix synthesis, and modulating inflammatory markers, leading to effective pain reduction [33]. However, challenges may arise in achieving stable differentiation into the desired tissue in specific environments due to the difficulty in precise differentiation control. To address these challenges, we utilized biomimetic inks derived from porcine bone and tendon decellularized extracellular matrix (dECM), supplemented with hydroxyapatite (HA) for the bone region and TGF- $\beta$ /poly(vinyl alcohol) (PVA) for the tendon region. These tissue-specific bioinks not only support cell proliferation and induce specific cellular differentiation of hASCs, but also provide suitable mechanical properties in the bone region and uniaxially aligned tendon tissue. Additionally, we used a bioprinting system equipped with a core-shell nozzle to effectively induce a gradient distribution of the engineered bone and tendon region without requiring any additional apparatus or complex procedures to fabricate the tendon-TBI-bone region. In the core region, we extruded the tendon-dECM-based bioink with hASCs, whereas in the shell region, we extruded the bone-dECM-based bioink. We fabricated a tendon/gradient TBI/bone construct by controlling the volume fractions of the core and shell regions. By selecting appropriate biological components and optimizing the volume extrusion rates in the core and shell nozzles, biomimetically engineered cell constructs that mimic the complex tendon-TBI-bone tissues can be created.

To evaluate the biofunctional results of the cell constructs, we performed *in vitro* testing to assess the influence of the engineered cell constructs on the expression of various genes related to osteogenic and tenogenic activities as well as their mechanical properties. Finally, we observed the effects of the engineered constructs laden with hASCs in an *in vivo* rabbit injured model of a full-thickness partial-width RCT.

## 2. Results and discussion

Functional biomaterials were used to formulate bone and tendon bioinks to fabricate complex tissue-mimetic cell constructs consisting of the bone, tendon, and TBI regions. Bone dECM (BdECM) and photocrosslinkable tendon dECM (TdECMA) were isolated from porcine tissues to provide tissue-specific microenvironments. Fig. 1A shows the formulations of the bone and tendon bioinks (bioink-B and bioink-T, respectively). Bioink-B contains BdECM (5 wt%) and hydroxyapatite (HA, 0.2 g/mL) to improve mechanical properties and accelerate the osteogenic differentiation of the embedded hASCs ( $2.0 \times 10^7$  cells/mL) [34–36]. For bioink-T, TdECMA (5 wt%) containing a photo-initiator (Irgacure2959, 3 wt%) was mixed with TGF- $\beta$  (10 ng/mL) as a tenogenesis-inducing factor [37,38] and polyvinyl alcohol (PVA, 0.1 g/mL) as a cell/collagen alignment-inducing component [39–41] to guide the cell alignment and induce a high degree of tenogenic differentiation of the laden hASCs.

The TBI area exhibited functionally graded anatomical and physiological microenvironments transitioning from a soft and flexible region to a stiff and mineralized region with an integrated and continuous structure containing diverse cell types and ECM components (Fig. 1B)

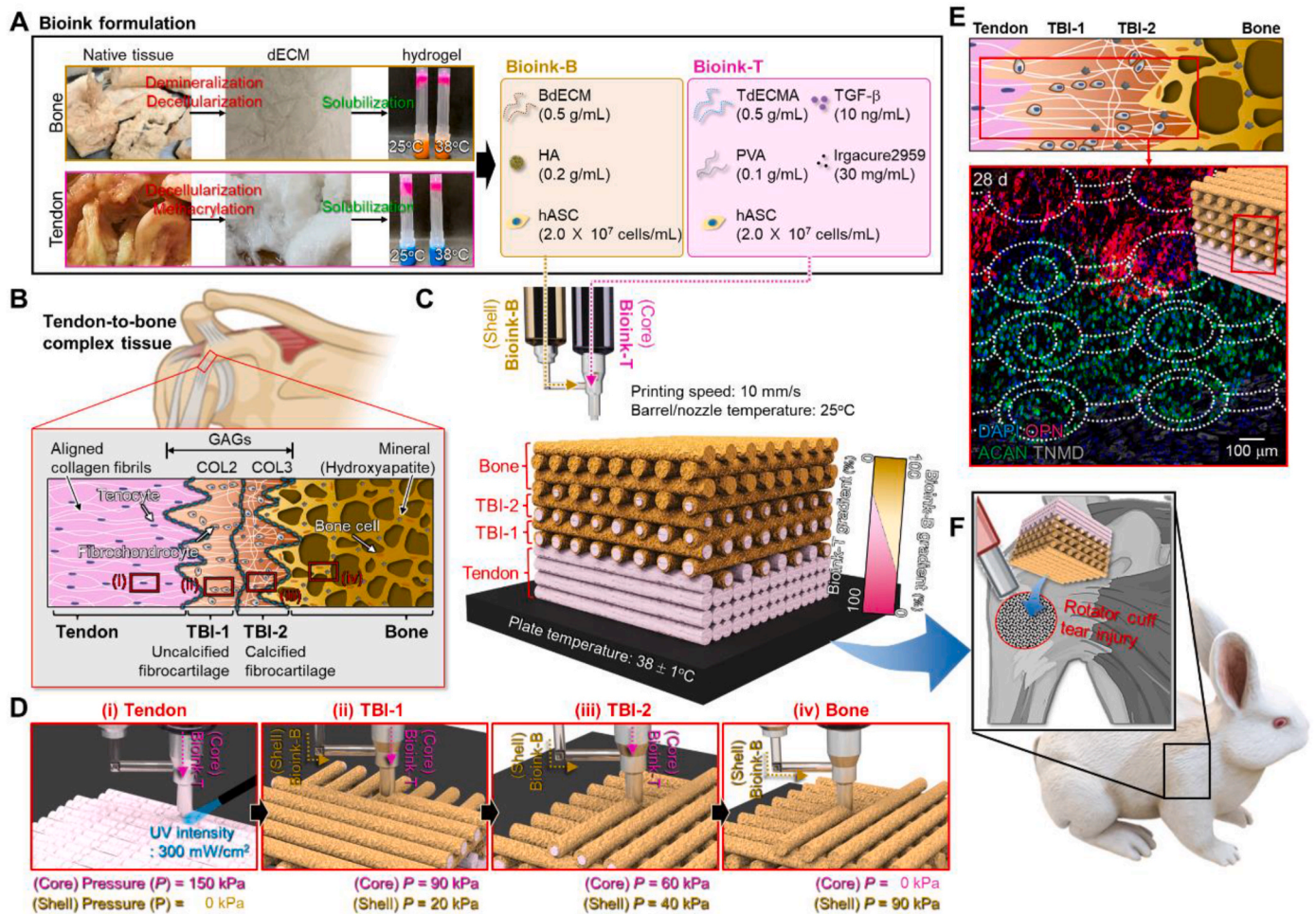


**Fig. 1.** Schematics of the bioprinting process for the tendon-to-bone complex structure. Schematics illustrating (A) the bone- and tendon-specific bioinks formation, (B) the native rotator cuff tissue structure, and (C) the bioprinting process for the tendon-to-bone structure with biologically graded tendon-to-bone interface (TBI). (D) Schematics demonstrating the applied pneumatic pressures for each tissue region. (E) DAPI (blue)/osteopontin (OPN, red)/aggrecan (ACAN, green)/tenomodulin (TNMD, white) image of the bioprinted complex structure at 28 d. (F) Schematic images demonstrating the *in vivo* evaluation using the rotator cuff tear model.

[1–4]. Generally, the TBI region can play an essential role in transferring mechanical stresses and maintaining joint stability; therefore, in this work, tendon-to-bone complex tissue with a partially graded TBI region was fabricated using a core-shell nozzle attached to the bioprinter and dECM-based bioinks (bioink-B and bioink-T, Fig. 1C).

To achieve this gradient structure, the appropriate volume fraction of the two bioinks was selected in each layer of tendon (thickness = ~1 mm), TBI-1 (bioink-B: bioink-T = 5:5, thickness = ~0.25 mm), TBI-2 (bioink-B: bioink-T = 7.5:2.5, thickness = ~0.25 mm), and bone (thickness = ~1 mm) by manipulating the pneumatic pressure applied to the core (bioink-T) and shell (bioink-B) regions, constantly maintaining a strut diameter of around 300  $\mu$ m to avoid cellular necrosis (Fig. 1D) [42]. Bioink-B and bioink-T were individually extruded onto the bone and tendon regions, respectively. In the bone region, bioink-B was printed in a normal mesh structure, whereas bioink-T in the tendon region was printed in uniaxially aligned tendon fibers, as shown in Fig. 1D [43,44].

The bioprinted cell construct with a gradient TBI region using hASCs was cultured for 28 days, and a well-developed tendon-TBI-bone structure was observed, which was evaluated using DAPI (blue)/osteopontin (OPN, red)/aggrecan (ACAN, green)/tenomodulin (TNMD, white) images (Fig. 1E). The components (HA and BdECM) in the bone region clearly induced osteogenic differentiation of stem cells, whereas the TGF- $\beta$  and TdECMA contents evoked tenogenic differentiation of the

cells. Furthermore, fibrocartilage, induced by the gradient bone-tendon structure, was well-formed in the TBI region. After fabricating the biomimetic bone-tendon structure, it was implanted into the defect region of a rabbit RCT model to assess its regenerative properties (Fig. 1F).

## 2.1. Preparation of bioinks for the bone and tendon tissues

Before fabricating the tendon-to-bone complex cell constructs, ECM-based bioinks for bone and tendon tissues were formulated to provide efficient biochemical environments for the osteogenic and tenogenic differentiation of stem cells, respectively [19,38,45,46]. Porcine tissue-derived bone dECM and tendon dECMA were used as the base hydrogels for each bioink. Moreover, bioceramic (HA) was added to bioink-B to provide additional mechanical and osteoinductive activities, and a cell-align-inducing biomaterial (PVA) and tendon-differentiation growth factor (TGF- $\beta$ ) of the stem cells were added to bioink-T.

As shown in the scanning electron microscope (SEM) image in Fig. 2A, nanoscale HA particles (approximately 1  $\mu$ m) were mixed with the BdECM hydrogel. In general, bioceramic-containing composite bioinks can clearly induce the osteogenic differentiation of hASCs [36, 47,48], whereas bioceramic particles can generate shear stress-based damage to the laden cells during the printing process. To control this cell damage, the proper composition of the bioceramic in the bioink should be selected. To determine the effect of bioceramics on various



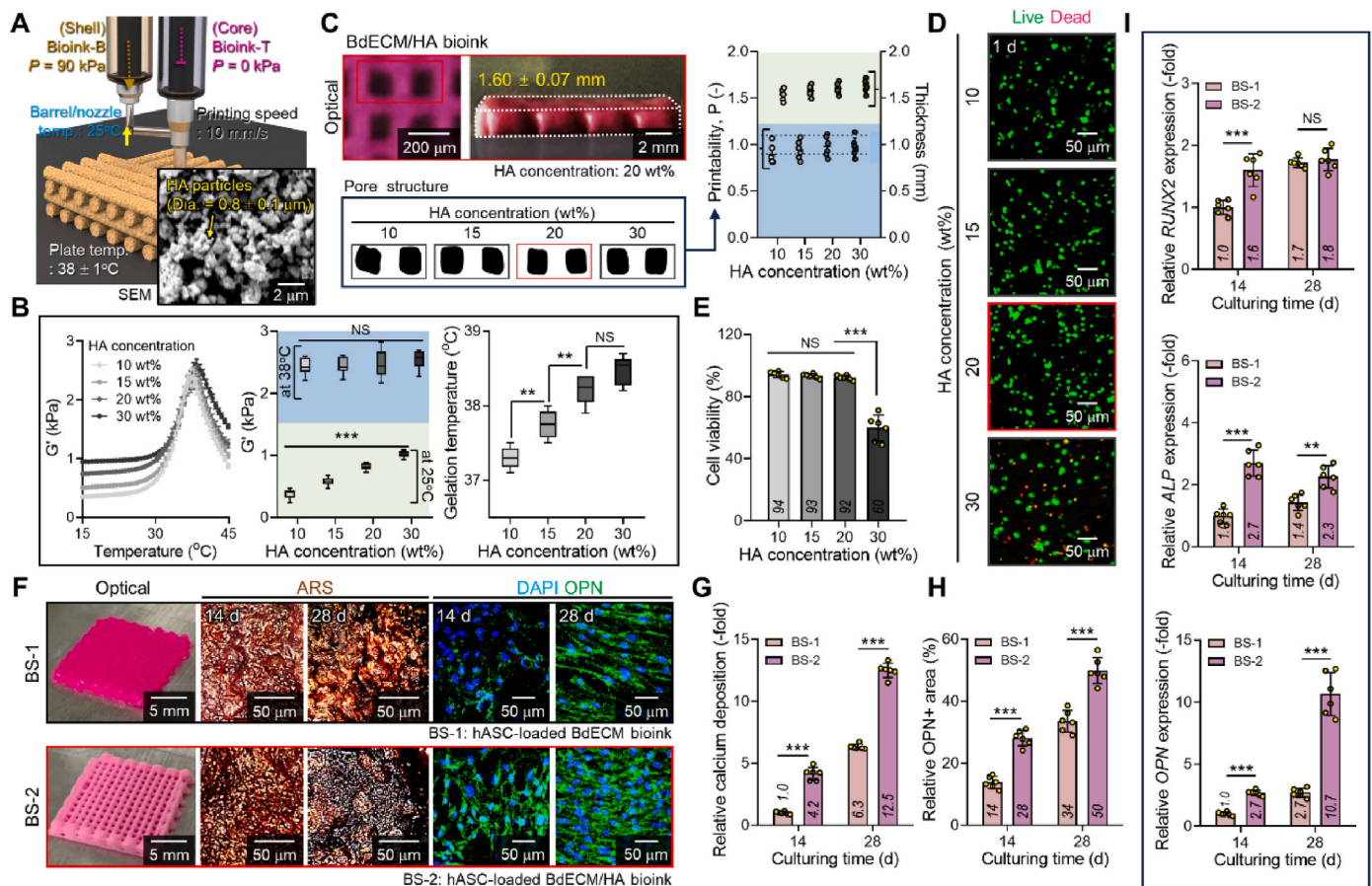


**Fig. 2. Preparation of bioink-B for the fabrication of the bone tissue.** (A) Schematic image illustrating the bioprinting process for the bone construct. (B) Rheological properties (storage modulus,  $G'$ ,  $G''$  at 25 and 38 °C, and gelation temperature for the bone-derived decellularized extracellular matrix (BdECM) and hydroxyapatite (HA) biocomposite bioinks with different HA concentrations (10, 15, 20, and 30 wt%) ( $n = 6$ ). (C) Optical images for the 3D mesh structures bioprinted using the bioink (20 wt% of HA contents) and quantitatively evaluated printability and thickness for the diverse bioinks ( $n = 6$ ). (D) Live (green)/dead (red) images for the bioinks after bioprinting process and (E) estimated cell viability ( $n = 6$ ). (F) Optical, Alizarin red S (ARS), and DAPI/OPN (red) images for the 3D bone structures bioprinted with hASC-laden BdECM naive bioink (BS-1) and bioink-B (BS-2). Quantitatively analyzed (G) relative calcium deposition and (H) OPN positive area of the BS-1 and -2 ( $n = 6$ ). (I) Expression of osteogenic differentiation-related genes at 14 and 28 d of culture ( $n = 6$ ). With the incorporation of HA particles into the BdECM-based bioink at a concentration of 20 wt%, the BS-2 biocomposite structure demonstrated significantly improved osteogenesis of hASCs compared to the naive BdECM construct. All values are presented as the mean  $\pm$  standard deviation (SD) (\* $p < 0.05$ , \*\* $p < 0.01$ , and \*\*\* $p < 0.001$ ).

biological and biophysical factors, different concentrations (10, 15, 20, and 30 wt%) of HA particles were added to the hASC-laden BdECM-based bioink (5 wt%) to observe their rheological properties, printability, and cellular activities.

A temperature sweep test was performed to observe the effect of HA on the rheological properties of the composite bioink (Fig. 2B). In general, to obtain a biologically safe and stable 3D shape-ability of the cell-laden construct, the bioink extruded through the microscale nozzle should flow under low shear stress (inducing the lowest cell damage), whereas after printing the cell struts, the printed struts should have a relatively higher viscosity to sustain the printed shape compared to the bioink passing through the nozzle [49]. Therefore, an appropriate printing temperature that affects bioink viscosity is required.

As shown in Fig. 2B, an increase in HA content enhances the storage modulus ( $G'$ ) of the biocomposites at 25 °C (before gelation of the BdECM hydrogel), while similar  $G'$  at gelation temperature was observed independent of the HA concentration, indicating a similar gelation degree of the matrix phase (BdECM hydrogel) (Fig. 2B) [50]. However, with increasing HA concentration, the gelation temperature inducing the maximum  $G'$  of the composite bioink was increased only slightly (Fig. 2B and S1A). This phenomenon could be due to the disturbance of HA particles in the collagen fibrillation rate of BdECM [36,50]. Based on the temperature sweep rheological results, we selected the proper

printing temperature for the lowest  $G'$  for the nozzle temperature and the highest  $G'$  at the printing stage for each composite bioink.

After selecting the printing temperature of the barrel and working plate, we printed composite bioinks with different HA contents (10, 15, 20, and 30 wt%). To observe the printability of the composite bioinks, mesh shapes consisting of printed struts were evaluated by observing their pore shapes. All the composite bioinks printed using the selected printing conditions showed acceptable printability ( $0.9 < \text{printability} < 1.1$ ) and reasonable mechanical strength (determined by the thickness of the stacked cell struts), independent of the HA concentration (Fig. 2C and S1B) [51].

Along with the printability of the composite bioink, the initial cell viability is an important criterion for the successful regeneration of target tissues. Fig. 2D shows live (green) and dead (red) cells at various HA concentrations. As shown in the results, up to 20 wt% HA in the bioink, the initial cell-viability at 1 day was very high (over 90 %), but severe cell damage (cell viability  $< 60$  %) was observed at 30 wt% HA (Fig. 2D and E) owing to the higher wall shear stress caused by the composite bioink containing 30 wt% HA in the microscale nozzle. In addition, we observed that the initial cell viability directly affected the osteogenic ability of stem cells, as determined by OPN immunofluorescence (at 14 days) (Figs. S1C and D). As evaluated by the OPN results, the osteogenic activity was the highest in the printed structure



containing 20 wt% HA. Therefore, we selected 20 wt% HA to formulate bioink-B.

To assess the osteogenic activity of bioink B, engineered bone structures with stable cell viability (>90 %), as shown in the live/dead images in Fig. 2F and S2A were fabricated under the following conditions (pneumatic pressure = 90 kPa, printing speed = 10 mm/s, barrel/nozzle temperature = 25 °C, and plate temperature = 37–39 °C) using two bioinks [hASC-loaded BdeECM bioink (BS-1) and proposed bioink-B (BS-2)] (Fig. 2F). In the 3-(4,5-dimethylthiazol-2-yl)-2,5-diphenyltetrazolium bromide (MTT) assay, BS-2 showed relatively improved cell growth compared to BS-1 after 1, 3, and 7 d of culture (Fig. S2B). The rapid cell proliferation can be attributed to the different morphological structures of BS-1 and BS-2. As shown in the SEM images shown in Fig. S2C, much larger pores (higher porosity) were observed in BS-2 compared to those in BS-1, which can affect the cell growth of the laden cells owing to effective cell-to-cell communication and efficient transport of nutrients [36]. Furthermore, the incorporation of the bioceramic particles into BdeECM-based bioconstructs clearly enhanced the compressive strength of the bone region (Fig. S2D) [36,50]. However, since the inclusion of HA particles was selected based on printability and cell viability to ensure a stable bioprinting process, further improvement in mechanical properties is still needed to better reflect native bone tissues in our future studies [52].

According to previous studies, when stem cells are cultured in osteogenic microenvironments, TGF- $\beta$ - and BMP-related signaling pathways including SMAD and MAPK can be activated, influencing both early and late state osteogenesis of stem cells (Fig. S2E) [53,54]. Likewise, introducing HA particles in the BdeECM-based bioink significantly activated TGF- $\beta$ - and FGF-related signaling pathways compared to the BS-1 without bioceramics, as validated through gene expression analysis at 7 days of culture (Fig. S2E). These results suggest that the BS-2 construct is likely to contribute to the efficient differentiation of hASCs into the osteogenic lineage [53,54].

After culturing the bioprinted structures, alkaline phosphatase (ALP) activity, mineralization, immunofluorescence imaging, and gene expression were analyzed to observe the osteogenic activity of the cells at 7, 14, and 28 d (Fig. 2F–I and 2E,F). In terms of ALP activity, hASCs bioprinted with HA particles exhibited greater enzyme activation than stem cells without bioceramics (Fig. S2E). In addition, more densely stained mineralized cells were observed in the Alizarin red S (ARS) staining images of BS-2, with improved deposition of calcium ions relative to those of BS-1 (Fig. 2F and G), indicating that the mineralization of hASCs was efficiently accelerated by the synergistic effects of the abundant biological microenvironments, including the ionic components from the HA particles [36,50,55]. In the same manner, expression of an osteogenic marker (OPN at 14 and 28 d) and genes [runt-related transcription factor 2 (*RUNX2*), *ALP*, *OPN*, and osteocalcin (*OCN*)] were also significantly improved in BS-2 compared to BS-1, as validated by quantifying the OPN + area and polymerase chain reaction (PCR) analysis (Fig. 2H,I and S2G). In detail, the expression of the earlier genes (*RUNX2* and *ALP*) was activated in the BS-2 group on day 14, followed by consistent upregulation of the later markers (*OPN* and *OCN*) until day 28 [56,57]. Based on the *in vitro* osteogenic activity results, we decided to use BS-2 to fabricate the bone structure, which would provide an improved osteogenic microenvironment.

Tendon tissue is composed of well-organized fibrous collagen bundles [43,44]. To achieve an aligned cell construct using the bioprinting process, PVA was introduced into the methacrylated tendon dECM bioink (TdeECMA) as a structural alignment-inducing factor, in accordance with our previous studies [39,40]. In summary, fibrillated PVA molecules can be oriented in a bioink by flow-induced extensional and shear forces generated within the microscale nozzle, guiding the direction of cells and TdeECMA molecules [39,40]. This organized structure was sustained after crosslinking TdeECMA through immediate UV treatment, followed by the leaching of PVA during the culture period.

Various concentrations (50, 100, and 150 mg/mL) of PVA were

added to the TdeECMA bioink to evaluate the cell alignment activity. All bioinks showed shear thinning behavior, but as the PVA content increased, enhanced rheological properties ( $G'$  and  $\eta^*$ ) were observed (Fig. 3A) [39]. After performing the bioprinting process with 42.4  $\mu$ L/min volume flow rate to obtain similar diameter (around 300  $\mu$ m), cellular viability and alignment were assessed by observing live (green)/dead (red) and DAPI (blue)/F-actin (green) images at 3 and 7 days, respectively (Fig. 3B–D and S3A). Low cell viability (<75 %) and actin filament formation ( $7 \pm 1$  %) were observed in the bioink with a relatively high viscosity (containing 150 mg/mL of PVA). In addition, cell alignment was not effectively induced in the low-viscosity bioink containing 50 mg/mL of PVA (Fig. 3D). Based on these results, 100 mg/mL of PVA was used to formulate the tendon-targeted bioink to achieve a uniaxially aligned 3D cell construct with high cell viability (>90 %).

In general, the alignment of the stem cells can directly affect the tenogenic differentiation of the cells because the spatial organization can affect the distribution and activation of growth factors and cytokines including TGF- $\beta$  and fibroblast growth factor etc [37,38,58–61]. TGF- $\beta$  concentration was set at 10 ng/mL based on the expression of tenogenic markers validated by assessment of immunofluorescence imaging and gene expression analysis (Fig. S3B) [37,38]. To assess the tenogenic activities, bioprinted structures were obtained using the optimized printing condition (pneumatic pressure = 150 kPa, printing speed = 10 mm/s, barrel/nozzle temperature = 25 °C, and plate temperature =  $38 \pm 1$  °C) with *in situ* UV cross-linking process (300 mW/cm<sup>2</sup>) (Fig. S3C). To further activate the tenogenic differentiation of hASCs, TGF- $\beta$  was added to the TdeECMA/PVA bioink and the 3D structure was printed to assess its effectiveness [37,38]. To compare the tenogenic activities and aligned tendon structures, the bioprinted cell constructs using the hASC-laden TdeECMA hydrogel (TS-1) and hASC-laden TdeECMA/PVA hydrogel (TS-2) were compared with the hASC-laden TdeECMA/PVA/TGF- $\beta$  hydrogel (TS-3).

Fig. 3E shows the optical, SEM, collagen type I (COL1), and DAPI/F-actin images of the bioprinted structures after 7 days. The PVA component in the bioinks clearly guided the alignment of collagen molecules in the bioinks, as shown in the SEM and COL1 images of the bioprinted tendon structures TS-2 and TS-3 and leached out during the culture period (Fig. 3E). Fourier-transform infrared (FT-IR) spectra shown in Fig. S3D, the absence of the PVA peak at 882 (C–C stretching), 916 (CH<sub>2</sub> rocking), and 1416 (CH<sub>2</sub> bending) cm<sup>–2</sup> in the TdeECMA/PVA mixture after 1 day of incubation, which was present in the initial state of the mixture, indicates that the PVA contents have leached out [39, 62]. Additionally, the initial mass change observed on the first day of incubation in the biodegradation results from Fig. S4 also supports the removal of PVA. hASCs exhibited high cell viability above 90 % in all bioconstructs, improved cellular proliferation was observed in the cell constructs fabricated with bioinks containing PVA compared with TS-1, indicating that the spaces left by the leached PVA can act as a pore structure for cell growth (Figs. S3E and F) [39,42]. In addition, as the supplemented growth factor also improved cellular proliferation, the TS-3 showed the highest cell proliferation rate due to the TGF- $\beta$  in the bioink which can be important in regulating cell growth, inflammation, and even tissue repair [37,38,63–65].

Following cultivation of the bioconstructs in the cell growth medium, DAPI/F-actin imaging was conducted to assess the morphologies of the bioprinted hASCs on day 7 (Fig. 3E). As expected, well-organized actin filaments of the cells were observed in the F-actin images of the TS-2 (orientation factor,  $f = 0.71 \pm 0.08$ ) and TS-3 ( $f = 0.71 \pm 0.06$ ) groups, whereas they were randomly distributed in the TS-1 ( $f = 0.25 \pm 0.18$ ) (Fig. 3F). These results provide evidence that the addition of the PVA component, which was aligned by carefully selected fabrication conditions, efficiently guided the embedded cells after the bioprinting process.

To assess tenogenic properties, DAPI/TNMD (red) imaging (at 14 and 28 days of culture) and gene expression analysis (at 28 days of

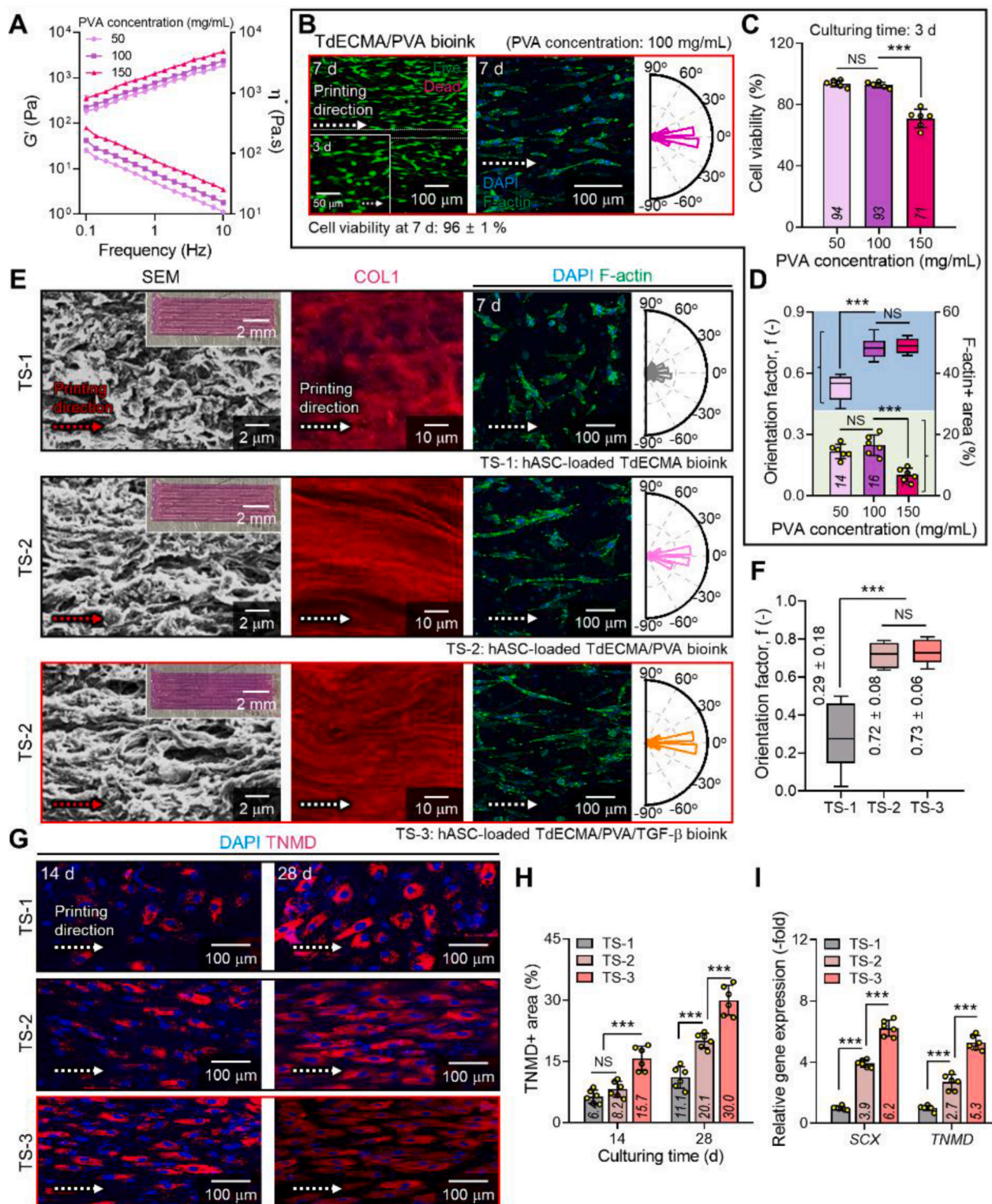


**Fig. 3.** Preparation of bioink-T for the fabrication of tendon tissue. (A) Rheological properties ( $G'$ ) for the tendon-derived dECM methacrylate (TdECMA)-based bioink containing diverse concentrations of the PVA (50, 100, and 150 mg/mL) ( $n = 6$ ). (B) Live/dead (at 3 and 7 d) and DAPI/F-actin (green) (at 7 d) images and quantified (C) cell viability, (D) orientation factor, and F-actin positive area for bioprinted structures using the TdECMA/PVA bioinks ( $n = 6$ ). (E) Scanning electron microscope (SEM), collagen type-I (COL1), and DAPI/F-actin (at 7 d) images for the tendon structures fabricated with TdECMA naive bioink (TS-1) and TdECMA/PVA-based bioinks with (TS-3) and without (TS-2) transforming growth factor beta (TGF- $\beta$ ). (F) Quantified orientation factor of the actin filament ( $n = 6$ ). (G) DAPI/TNMD images and quantitatively analyzed (H) TNMD positive area and (I) tenogenesis-related gene expression for the bioprinted tendon constructs ( $n = 6$ ). The synergistic effects of cellular alignment and tenogenic molecules in TS-3 significantly improved the differentiation of hASCs into the tenogenic lineage compared to TS-1 and TS-2. All values are presented as the mean  $\pm$  SD (\*\* $p < 0.01$  and \*\*\* $p < 0.001$ ).



culture) were conducted on the cell constructs (Fig. 3G–I). Because TNMD-expressing cells were observed in all bioprinted constructs after 14 and 28 days of culture, the aligned hASCs expressed significantly higher levels of tenogenic markers with improved TNMD-positive areas (Fig. 3H). In particular, tendon structure (TS-3) containing TGF- $\beta$  showed the highest TNMD expression. Similar to the immunofluorescence imaging results, efficiently upregulated expression of the tenogenic differentiation-related genes scleraxis (SCX) and TNMD was also observed in TS-3 cells (Fig. 3I). This enhancement in tenogenesis-related gene expression is likely attributed to the synergistic effect of the successfully aligned structures and bioactive molecules. These synergistic effects significantly improved the activation of hASC's TGF- $\beta$ - and BMP-related signaling pathways, such as SMAD and MAPK, leading to the

induction of tenogenic gene expression, as validated by gene expression analysis after 7 days of culture (Fig. S3G) [53,66]. These results indicated that the combination of cellular orientation cues and bioactive components synergistically influenced tendon formation in hASCs. Based on these results, the TS-3 bioink was selected as bioink-T.

After the selection of the bioink-B and -T, bioprinted structures (BS-2 and TS-3) were incubated in a culture medium and collagenase solution (0.1 U/mL) to assess the structural stability and biodegradation ability (Fig. S4). TS-3 showed rapid degradation at 1 day, which appears to be due to PVA leaching. After 28 days, it exhibited degradation levels of  $67 \pm 4\%$  and  $86 \pm 4\%$  in medium and collagenase solution, respectively. In contrast, BS-2, due to the HA component, showed degradation rates of only  $9 \pm 1\%$  and  $13 \pm 1\%$  after 28 days. The bioprinted 3D constructs

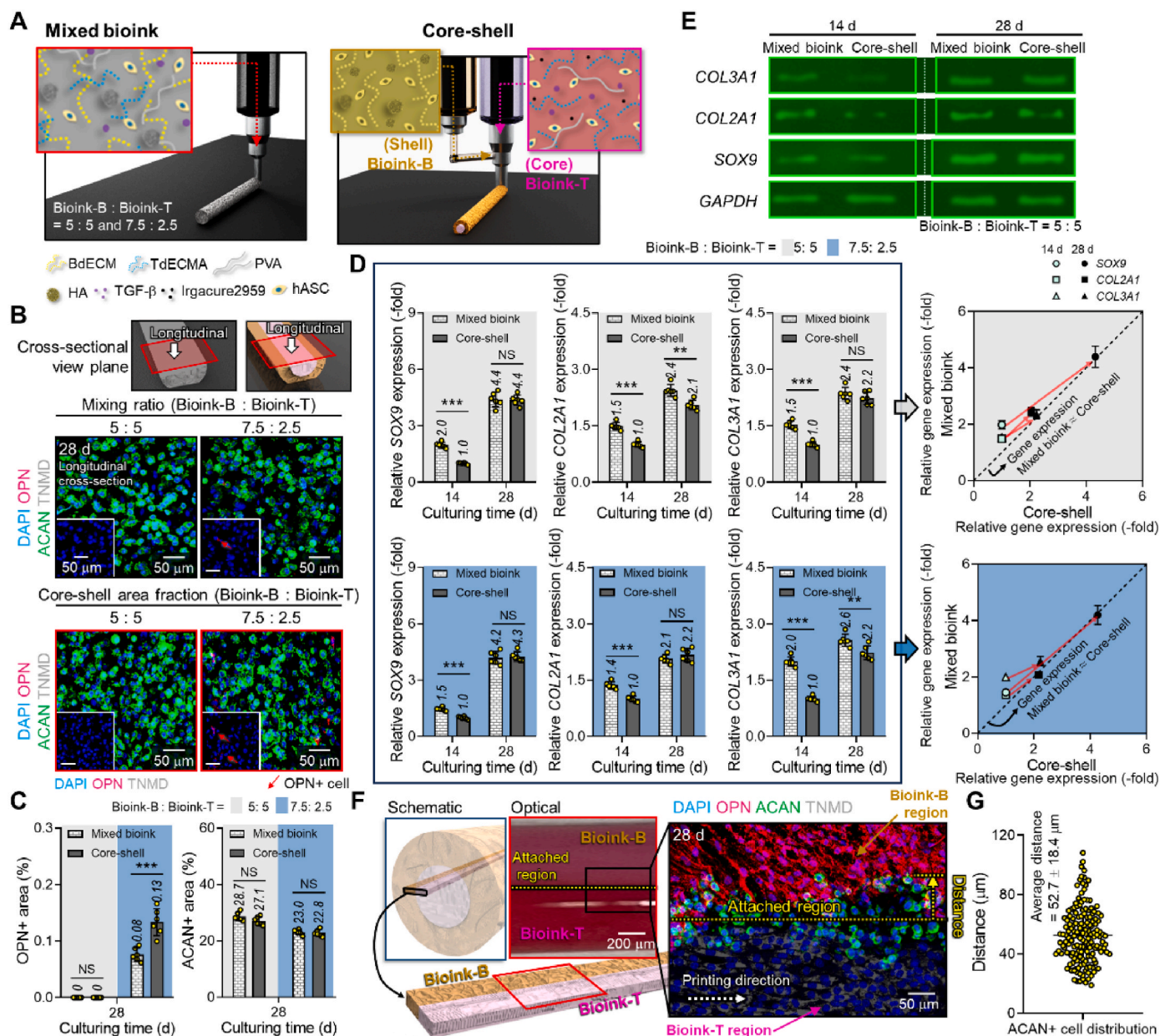


**Fig. 4.** Chondrogenic differentiation of hASCs in the mixture of bioink-B and -T. (A) Schematics demonstrating the bioprinted fibrocartilage structures using mixture of bioink-B and -T and core (bioink-T)-shell (bioink-B) nozzle. (B) DAPI/OPN/TNMD/ACAN (at 28 d) images and (C) quantified ACAN, TNMD, and OPN positive areas for the bioprinted mixture of bioink-B and -T at the ratios of 5:5 and 7.5:2.5 ( $n = 6$ ). (D) Gene expression ( $n = 6$ ) and (E) agarose gel-based electrophoresis for RT-PCR analyses of the SOX9, COL2A1, and COL3A1 in the core-shell and mixed structures of bioink-B and -T at 14 and 28 d. (F) Schematic and DAPI/OPN/ACAN/TNMD images and (G) quantified distance of the ACAN-positive hASCs distribution apart from the attached region of both bioinks ( $n = 160$ ). Bioprinting of TBI tissues with the core-shell nozzle resulted in fibrocartilage formations similar to those achieved with traditionally bioprinted structures using mixed bioinks. All values are presented as the mean  $\pm$  SD (\*\* $p < 0.01$  and \*\*\* $p < 0.001$ ).



were fully degraded in collagenase at 28 days, while those maintained their structure in the culture medium (Fig. S4B). Based on the results, we can carefully estimate that bioink-B and bioink-T can be effectively utilized to obtain tendon-to-bone tissues for regenerative applications, as they provide stable 3D structures and appropriate biodegradable conditions.

## 2.2. Fabrication of the gradient TBI region using bioinks

After the formulation of the bone- and tendon-targeted bioinks, a fabrication method using a core-shell nozzle-supplemented bioprinting process was designed to obtain the gradient TBI region. Since the biological components in bioink-B and bioink-T clearly showed the osteogenic and tenogenic lineages of hASCs, we expected that the combination of these bioinks could induce the formation of fibrocartilage tissue [14,26]. In this study, bioink-B and bioink-T were printed using a core/shell (bioink-T/bioink-B) nozzle to obtain mixed struts consisting of both bone- and tissue-specific bioactive factors for the TBI structure using an easy and versatile process without a complex fabrication procedure, such as rapidly changing several printing barrels containing each bioink and mixed bioink.

To observe the efficacy of the core-shell structured TBI, their chondrogenic capacities were assessed by conducting immunostaining imaging and qRT-PCR analysis. In recent, various researchers have reported biofabrication strategies to achieve tendon-to-bone complex tissues, including embedding cell-laden bioinks into frames with gradient bioceramic components [67,68], directly attaching tendon and bone constructs [11,24], preparing additional chondrogenic bioinks [25,27], and formulating mixtures of tendon and bone bioinks [12,14,26]. Among these methods, the use of mixed tendon and bone bioinks can achieve a gradually transitioning TBI region [14,26]. Therefore, to assess the efficacy of the core-shell structures proposed in this study, mixtures of bioink-B and bioink-T were bioprinted to compare cellular responses with those of the core-shell structure. Mixtures of the bioink-B and -T (5:5 and 7.5:2.5) were bioprinted to compare the fibrocartilage formation of core-shell structures (area fraction of bioink-B: bioink-T = 5:5 and 7.5:2.5) *in vitro* (Fig. 4A). Interestingly, the ACAN + cells in the core-shell structure were similar to the struts bioprinted with a mixture of bioink-B and bioink-T at volume fractions of 5:5 and 7.5:2.5, respectively (Fig. 4B and C). In addition, although the expression of SRY-box transcription factor 9 (*SOX9*), collagen type II (*COL2A1*), and collagen type III (*COL3A1*) genes was more accelerated in the mixed bioinks at 14 d, differentiation of hASCs in the core-shell structures kept pace with those in the mixture during the 28 d at ratios of 7.5:2.5, and 5:5, respectively (Fig. 4D and E). Based on these results, although the core-shell structure cannot be perfectly similar to the mixed bioinks, we suggest that the proposed core-shell structure of the TBI region could mimic the well-mixed structure to some extent. The core-shell nozzle allows for the creation of a multi-layered structure with four regions of different compositions without the need to replace barrels or nozzles during the process, unlike the application of mixed bioink [14,26]. This method can more accurately replicate a gradient TBI structure and facilitate effective fibrocartilage differentiation of stem cells.

The following experiment was conducted to confirm the possibility of hASC differentiation in the fibrocartilage region, which could be obtained through the contact area between the printed core (bioink-T) and the shell strut (bioink-B) through the core-shell nozzle. As shown in Fig. 4F, bioink-B and bioink-T were printed in parallel, such that the printing areas were in contact with each other. As can be seen from the results of DAPI/OPN/ACAN/TNMD on 28 d, it was found that fibrocartilage regions (up to  $52.7 \pm 18.4 \mu\text{m}$  away from the attached line, Fig. 4G) were well formed in the contacting region. We believe that these results can be attributed to the interaction between bioink-B for bone regeneration and bioink-T for tendon regeneration. This simple assessment suggests that the core-shell struts of both bioinks could adequately develop TBI composed of fibrocartilage tissue.

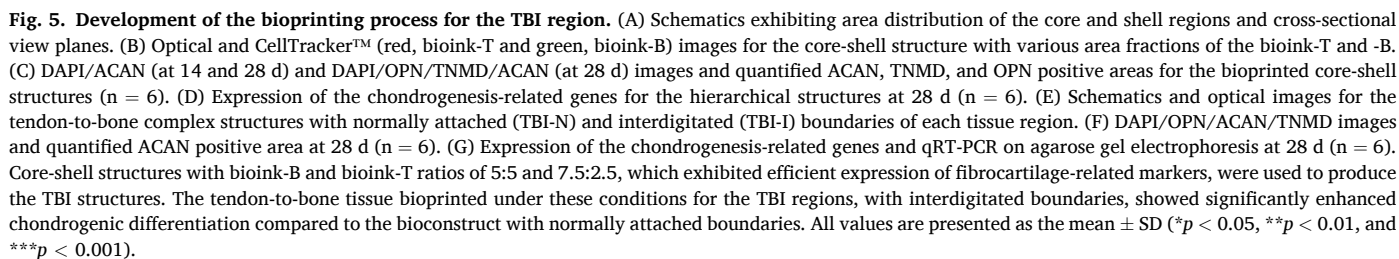
To achieve TBI constructs with graded biological components more efficiently, the chondrogenic activities of struts with diverse area ratios (bioink-B: bioink-T = 3:7, 3.5:6.5, 4.5:5.5, 5:5, 7.5:2.5, and 8.5:1.5) for the core and shell regions were assessed using immunofluorescence imaging and PCR analysis. The volume flow rates for the core and shell regions were manipulated to obtain different area fractions for struts with similar diameters (approximately 300  $\mu\text{m}$ ) (Fig. S5). To visualize the distribution of immunofluorescence-positive cells within the core-shell struts, we observed the perpendicularly and longitudinally sliced cell constructs, as illustrated in the schematics. (Fig. 5A).

To observe the cell distribution within the struts printed using the core-shell nozzle, red- (core) and green-colored hASCs (shell) were printed with various designed area fractions (Fig. 5B). As shown by the red and green colors of the cross-sectioned struts, the cells were well positioned in each region. After 14 and 28 days of culture, immunofluorescence imaging (DAPI/aggreCAN (ACAN) and DAPI/OPN/ACAN/TNMD) of the surface and longitudinal cross sections of the struts was performed to evaluate the chondrogenic differentiation of the bioprinted hASCs (Fig. 5C). Interestingly, ACAN-stained cells were widely observed in all printed struts, independent of the bioink ratio. As reported in previous studies, stem cells successfully differentiated into a fibrochondrogenic lineage within a mixture of dECM-based bone- and tendon-specific bioinks [14,26]. Similar to previous studies, fibrochondrogenic differentiation of bioprinted hASCs in the core-shell structures could have been induced by the synergistic effects of the biochemical cues of bioink-B and bioink-T. However, the degree of the ACAN-stained area, indicating the fibrocartilage region, was highly dependent on the mixture ratio. As the bioink-B fraction increased, the ACAN-positive area increased; however, after reaching a certain threshold at a volume fraction of 5:5, the ACAN region decreased (Fig. 5C(i)). Furthermore, as shown in the longitudinal cross-sectional images, the TNMD-positive cells increased with increasing bioink-T fraction, while OPN-positive cells increased with increasing bioink-B fraction (Fig. 5C (ii, iii)). In addition, the behavior of the positive ACAN area was similar to that of the strut surface (Fig. 5C(iii)).

These staining results indicate that the fabrication of core-shell structures consisting of appropriate fractions of the selected tendon- and bone-specific bioinks can induce chondrogenic differentiation of the embedded cells. However, because these cells cannot adequately receive biological cues from the bioink beyond a certain distance, results related to chondrogenic differentiation can be restrained by the designed geometry of the printed structure.

In addition, ACAN and *SOX9* genes were observed, and their expression was consistent with the immunostaining results (Fig. S6A). To assess the calcified and uncalcified fibrocartilage regions, we measured the expression of fibrocartilage region-related genes. Fig. 5D shows the expression of uncalcified fibrocartilage region-related genes, *COL3A1* and decorin (*DCN*), and calcified TBI region-related genes, *COL2A1* and collagen type X (*COL10A1*) [1–3,69]. Interestingly, we observed two unique core-shell mixture ratios (bioink-B: bioink-T = 7.5:2.5 and 5:5) and showed the highest expression in the calcified and uncalcified regions, respectively. Furthermore, the expression of OPN and TNMD was also evaluated to observe the osteogenic and tenogenic differentiation of the hASCs for various core-shell mixture ratios, by relatively comparing with the cells cultured within the pure bioink-B and bioink-T (set as “1”) structures (controls) (Fig. S6B). The core-shell structures mixed with various bioink ratios showed significantly decreased osteogenesis and tenogenesis compared to the controls. From the results, we can carefully estimate that the core-shell structures consisting of the two different bioinks can be affordable to mimic the gradient TBI region, and also we can select that the core-to-shell ratios of 5:5 (TBI-1) and 7.5:2.5 (TBI-2) of bioink-B and bioink-T were chosen to print the TBI regions (uncalcified and calcified region in fibrocartilage area), respectively.

In accordance with previous studies, when stem cells are cultured under the tenogenic microenvironments, several signaling pathways



signaling pathways compared to the negative control (TS-1 construct), as validated through gene expression analysis at 7 days of culture (Figs. S7B and C). Based on these results, the selected core-shell structures are expected to contribute to the effective formation of the TBI region in tendon-to-bone tissue through enhanced fibrocartilage



formation.

After selecting the bioink composition in the TBI region, the entire structure consisting of the tendon, TBI, and bone tissues was fabricated with two different contact types between the tendon and TBI region: normal contact boundary (TBI-N) and interdigitated contact boundary (TBI-I), as shown in the schematic images (Fig. 5E). Briefly, the regions where the tissue changed, such as the boundary between the tendon and TBI-1, were created by alternately printing bioink-T and TBI-1 to form a hybrid structure of interdigitated contact boundaries, as shown in the schematic and optical images. After 28 days, immunostaining was performed on the TBI-N and TBI-I structures to observe the interfacial tissue formation (Fig. 5F). While both types of interfaces expressed ACAN on day 28, more ACAN<sup>+</sup> cells were observed in TBI-I, consisting of a more finely divided interface region resembling a pattern similar to that of a natural continuous TBI. As shown in Fig. 5G, the expression of TBI-related genes and PCR products separated on the agarose gel via electrophoresis, including *ACAN*, *SOX9*, *COL2A1*, *COL3A1*, and *COL10A1*, was also significantly improved in the TBI-I group compared to the TBI-N group. These results suggest that TBI tissues can be obtained more effectively by fabricating an appropriately designed interface between the tendon and bone tissues.

### 2.3. In vitro cellular activities

Because TBI-I exhibited an improvement in the formation of fibrocartilage tissue in the TBI region compared to the normally contacted interfaces of TBI-N, it was selected to fabricate the tendon-to-bone complex tissue as the experimental group (Exp) (Fig. 6A). To compare the formation of tendon-to-bone tissue and the regenerative potential of Exp, a bioprinted control structure consisting only of tendon and bone layers without an artificially designed TBI region was used as BpC (Fig. 6A).

Optical images showed the bioprinted tendon-to-bone complex tissues with and without the TBI region (Fig. 6B). As shown in the CellTracker™ images, different distributions of the cells in bioink-T and bioink-B in the control and experimental structures were visualized by red- and green-stained hASCs, respectively (Fig. 6C). In particular, for the experimental group, the green cells in the shell region (bioink-B) and red cells in the core region (bioink-T) were well positioned, indicating that the designed core-shell structure in the TBI region was successfully obtained. Likewise, while bioink-T (weak ARS staining) and bioink-B (intensive ARS staining) were distributed separately in each region of the BpC, the cross-sectional images of TBI-1 and TBI-2 tissues in the Exp showed a weaker ARS-stained core and an intensively ARS-stained shell (Fig. S8A). Consistent with the CellTracker™ images, the core and shell regions differed in size between TBI-1 and TBI-2. Furthermore, the cross-sectional SEM images of the TBI structure in the Exp revealed a core region containing fibrous TdECMA and a shell region with HA particles and fibrous BdeECM (Fig. S8A). Thermogravimetric analysis (TGA) results supported the imaging observations, showing different HA contents in the tendon, TBI-1 (~48.8 %), TBI-2 (~67.2 %), and bone (~80.7 %) regions of the Exp, with HA content increasing from tendon to bone, as expected (Fig. S8B). The total HA content in the bioprinted BpC (41.5 %) and Exp (42.1 %) was similar (Fig. S8C).

After 28 days, immunofluorescence imaging of OPN, ACAN, and TNMD was performed on differentiated hASCs distributed in each layer of BpC and Exp (Fig. 6D). Briefly, the top and bottom layers of the structures were examined to visualize the OPN- and TNMD-stained cells distributed in the bone and tendon regions, respectively. In addition, ACAN<sup>+</sup> cells were visualized by observing the horizontally sliced cell constructs, as illustrated in the schematics (Fig. 6D). As shown in the images, well-differentiated hASCs stained with OPN (red) and TNMD (red) were observed in the top (bone) and bottom (tendon) layers of each group, respectively, exhibiting similar OPN<sup>+</sup> (BpC:21 ± 2 % and Exp:22 ± 2 %) and TNMD<sup>+</sup> (BpC:24 ± 4 % and Exp:25 ± 4 %) areas (Fig. 6E). However, in the case of ACAN (green) images, the tendon-to-bone

complex tissue containing graded TBI exhibited a significantly greater ACAN<sup>+</sup> area (27 ± 4 %) in the interface layer than in the BpC group (8 ± 1 %) (Fig. 6E). In addition, by observing the OPN (red)/ACAN (green)/TNMD (white) staining images of the vertically sliced cross-sections, a broader TBI layer distributed with ACAN-positive cells was found in Exp than in BpC (Fig. 6F). The immunostaining results indicated that the hASCs loaded in the core-shell structure of bioink-T and bioink-B successfully formed a broader TBI region *in vitro*, whereas only hASCs were distributed within a narrow range around the boundary between the tendon and bone structures expressing ACAN.

To further evaluate the formation of the tendon-to-bone complex tissue, qRT-PCR analysis was performed to assess the expression of genes related to the fibrocartilage, bone, and tendon tissues (Fig. 6G). Similar to the immunostaining results, the expression of fibrocartilage-related genes, including *ACAN*, *SOX9*, *COL2A1*, *COL3A1*, and *COL10A1* was significantly higher in Exp than in BpC. The expression of fibrocartilage-related genes was also validated by the similar observations of separated PCR products on the agarose gel electrophoresis (Fig. 6H). Despite the fibrocartilage-related genes, slightly higher expression of tenogenesis-related (*SCX* and *TNMD*) and osteogenesis-related (*OCN* and *OPN*) genes was observed in the BpC group (Fig. 6G). The lower expression of tenogenic and osteogenic differentiation-related genes in Exp was attributed to reduced tendon and bone portions owing to the formation of a broad TBI region.

Because the tendon-to-bone tissue interface can serve a function related to mechanical loads, the mechanical properties of the complex structures should be improved after the formation of the TBI region [1–3]. Therefore, the mechanical properties of the BpC and Exp groups were assessed after 3, 14, and 28 days of culture (Fig. 6I–K). The 'Z'-shaped bioconstructs containing elongated bone and tendon regions were prepared to conduct the tensile testing. During the bioprinting procedures, additional PET films were used to support the overhanging part of elongated bone region and removed prior to cultivation and measurement (Fig. 6I). To perform the tensile test, the elongated tendon and bone constructs were anchored from both ends without any supporting structures and stretched at a speed of 0.1 mm/s, as shown in Fig. 6I. During the progression of stretching, a mechanical force seemed to be loaded on the TBI region, and the mechanical properties increased as stem cell differentiation proceeded during the culture period (Fig. 6J). However, when comparing both complex structures, Exp tissue containing a graded TBI region showed a meaningfully reinforced maximum load and elastic stiffness compared to the BpC group (Fig. 6K). This result was corroborated by the immunofluorescence and gene expression results, indicating that the well-developed TBI tissue within the biologically graded tendon-to-bone unit exhibits potential as a mechanical support structure.

### 2.4. Evaluation of RCT restoration in vivo

To assess the regenerative capability of the biologically graded tissue, an RCT rabbit model in which the full-thickness partial-width RCT (FTPWRCT) was generated in the tendon-to-bone tissues of the right supraspinatus tendon to implant the bioprinted structures through a surgical experiment (Fig. 7A). The animals were randomly divided into four groups: Tear (no treatment and repair), Repair (repair without treatment), BpC (implantation of BpC structure), and Exp (implantation of Exp tissue). Animals without RCT were used as controls (CTL).

Eight weeks post-transplantation, the supraspinatus tendon (ST)-to-proximal humerus (PH) was separated from the rabbit arms to evaluate rotator cuff tissue regeneration. After rotator cuff injury, the mechanical properties of the TBI area can serve as crucial markers to confirm the quality of recovery of the rotator cuff tissue and its function [2,26]. Fig. 7B shows the load-distance curves of the Tear, Repair, BpC, and Exp groups. The optical images captured during the tensile test of Exp indicated that the stretching force was loaded onto the interface region of the tendon and bone tissues (Fig. 7C). As shown in the results of the



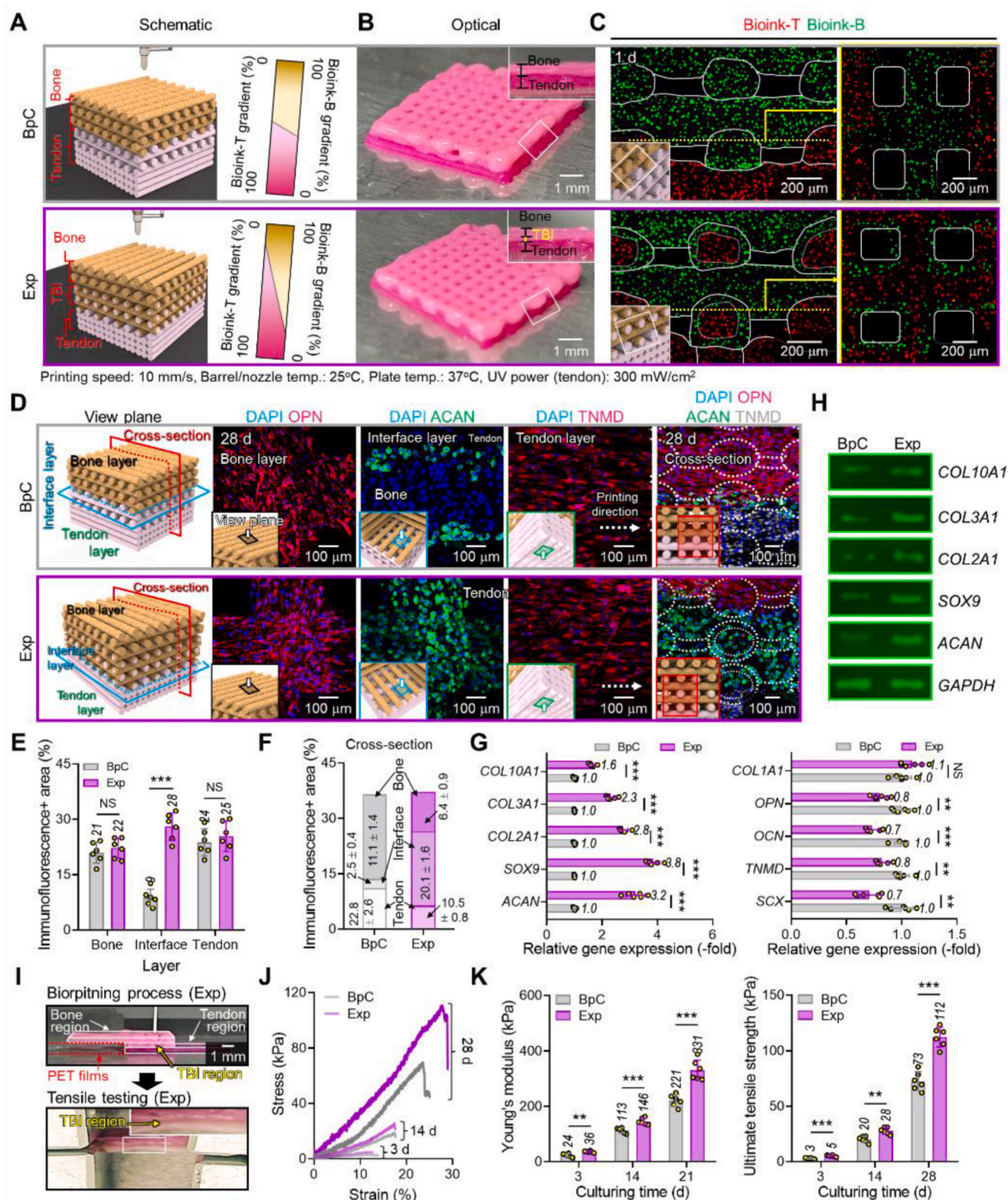


**Fig. 6.** *In vitro* cellular activities of the tendon-to-bone constructs. (A) Schematic, (B) Optical, and (C) CellTracker™ images for the bioprinted biomimetic complex tissues with (Exp) and without (BpC) biologically graded TBI structures. (D) OPN, ACAN, and TNMD immunofluorescence images for the bone, interface, and tendon layers and cross-section of the BpC and Exp structures at 28 d. Quantified (E,F) OPN, ACAN, and TNMD positive areas and (G) gene expression at 28 d (n = 6). (H) qRT-PCR conducts related to the chondrogenesis on agarose gel electrophoresis. (I) Optical images demonstrating the evaluation of the complex structures under tensile mode. (J) Tensile stress-strain curves and (K) estimated Young's modulus and Ultimate tensile strength at 3, 14, and 18 d (n = 6). The biomimetic complex tissue containing graded TBI structure exhibited significantly improved fibrocartilage formation and mechanical properties compared to the control, which lacked gradation. All values are presented as the mean ± SD (\*p < 0.05, \*\*p < 0.01, and \*\*\*p < 0.001).

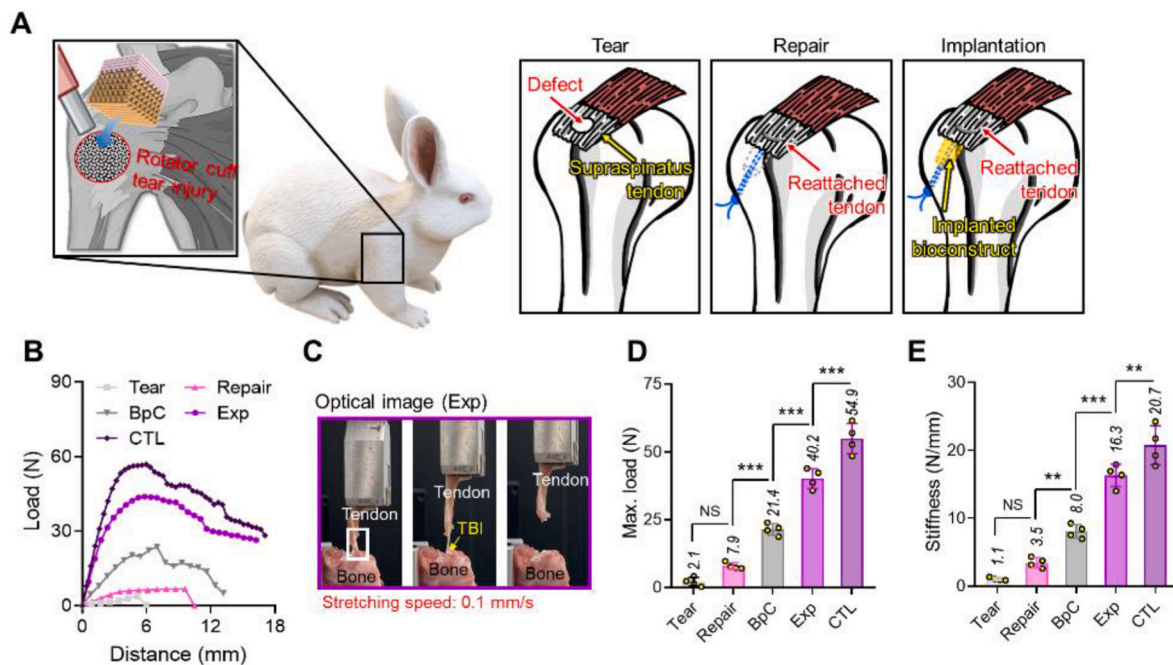


**Fig. 7.** Restoration of the rotator cuff mechanical properties after implantation of the bioconstructs *in vivo*. (A) Schematic for the surgical *in vivo* experiments using the rotator cuff tear injured rabbit model, including tear (RCT without implants and self-repair), Repair (RCT without implants and with self-repair), BpC (RCT with BpC implantation), and Exp (RCT with Exp implantation) groups. (B) Load-distance curves evaluated 8 weeks post-transplantation ( $n = 4$ ). (C) Optical images exhibiting the biomechanical testing for the Exp group. Quantitatively estimated (D) maximum load and (E) stiffness for each group ( $n = 4$ ). Implantation of Exp complex structures in the rabbit RCT model resulted in the greatest biomechanical improvements. Values are presented as the representative results for the load-distance curves and the mean  $\pm$  SD for the estimated maximum load and stiffness (\* $p < 0.05$ , \*\* $p < 0.01$ , and \*\*\* $p < 0.001$ ).

biomechanical tests, the bioconstruct-implanted groups showed significantly improved mechanical properties compared to the Tear and Repair groups. In particular, the highest maximum load and stiffness were observed in the RCT model treated with the biologically graded bioconstructs, while those were still lower than the native tissue (CTL group) without RCT injury (Fig. 7D and E). The results indicated that repairing the RCT model by treating the Exp structure facilitated mechanical function restoration of the TBI region, suggesting the effectiveness of biologically graded rotator cuff bioconstructs containing stem cells for the therapeutic regeneration of the complex tissue.

To observe the formation of new full-thickness tissues in the RCT space in each group, histological analyses including hematoxylin and eosin (H&E), safranin O (SO), Masson's trichrome (MT), and Sirius red (SR) imaging were performed on sections of the isolated tissues (Fig. 8). As shown in the histological images, the formation of well-organized collagen-rich tissue was observed in the BpC and Exp groups at 8 weeks post-implantation, exhibiting proper re-connection between the ST and PH tissue, while shortcomings in tissue remodeling were observed in the RCT models without treatment of the bioconstructs (Tear and Repair group) (Fig. 8A). In addition, hASC-loaded constructs influenced the presence of newly formed fibrocartilage tissue layers in the healing space compared with the Tear and Repair groups. Relative to the other groups, the Exp group formed a higher-quality TBI similar to the native tissue (CTL), characterized by fibrocartilage layers rich in proteoglycans containing rounded fibrochondrocytes and a tidemark at the gradient interface. In particular, the semi-quantitatively analyzed SO staining expression score was the highest in the Exp group, similar to the score of the CTL group relative to the other groups (Fig. 8B). As shown in the MT and SR images, the Exp group formed a densely organized collagen fibers relative to the other groups (Fig. 8C). Green-positive cells in SR images were abundant in the Exp group. Similarly, the highest semi-quantified MT and SR expression was observed in the Exp group (Fig. 8D and E). These observations revealed notable regeneration not only of the tendon and bone tissues, but also of TBI following treatment

with biologically graded structures.

To further investigate the contribution of the implanted bioconstructs to rotator cuff regeneration, immunohistochemical (IHC) imaging was performed on the retrieved RCT tissues (Fig. 9). Fig. 9A exhibits COL1, COL3, platelet endothelial cell adhesion molecule 1 (PECAM-1), and vascular endothelial growth factor (VEGF) images for the Tear, Repair, BpC, Exp, and CTL groups. Similar to the histological evaluation results, the expression of all IHCs was significantly upregulated in the treatment groups compared to the Tear and Repair groups. Additionally, the Exp structure efficiently improved tendon-to-bone tissue formation with TBI and angiogenesis, with the highest scores for COL1, COL3, PECAM-1, and VEGF (Fig. 9B–E). The significantly improved levels of PECAM-1 and VEGF in the BpC and Exp groups compared to the CTL (healthy group without RCT) suggest that our interventions may have shown the healing response by promoting angiogenesis and tissue remodeling. As Col1 and Col3 play crucial roles in tendons as the primary structural protein and during the early stages of tendon healing, respectively, the expression of Col1 and Col3 indicates the activation of repair responses and the growth of new tissue [72,73]. Elevated levels of Col3 suggest an enhancement in the regeneration process, as Col3 is initially increased but is gradually replaced by Col1 during the maturation phase. Based on previous studies, relative to the uninjured tissues (CTL), the deposition of new collagen fibers can result in higher levels of Col1 and tendon restoration shows an initial increase in Col3 content [72,73]. Additionally, while the differences in SO staining between Exp and BpC are not statistically significant, collagen protein formation is significantly higher in the Exp group. The increased expression of Col1 in the Exp group may be attributed to enhanced matrix remodeling and fibrocartilage formation at the tendon-bone interface, which may not directly correlate with the SO staining intensity in a statistically significant manner. These differences underscore the complexity of tissue remodeling processes, where different markers can exhibit varying degrees of change depending on the specific aspects of tissue repair and regeneration being evaluated. Further studies will be



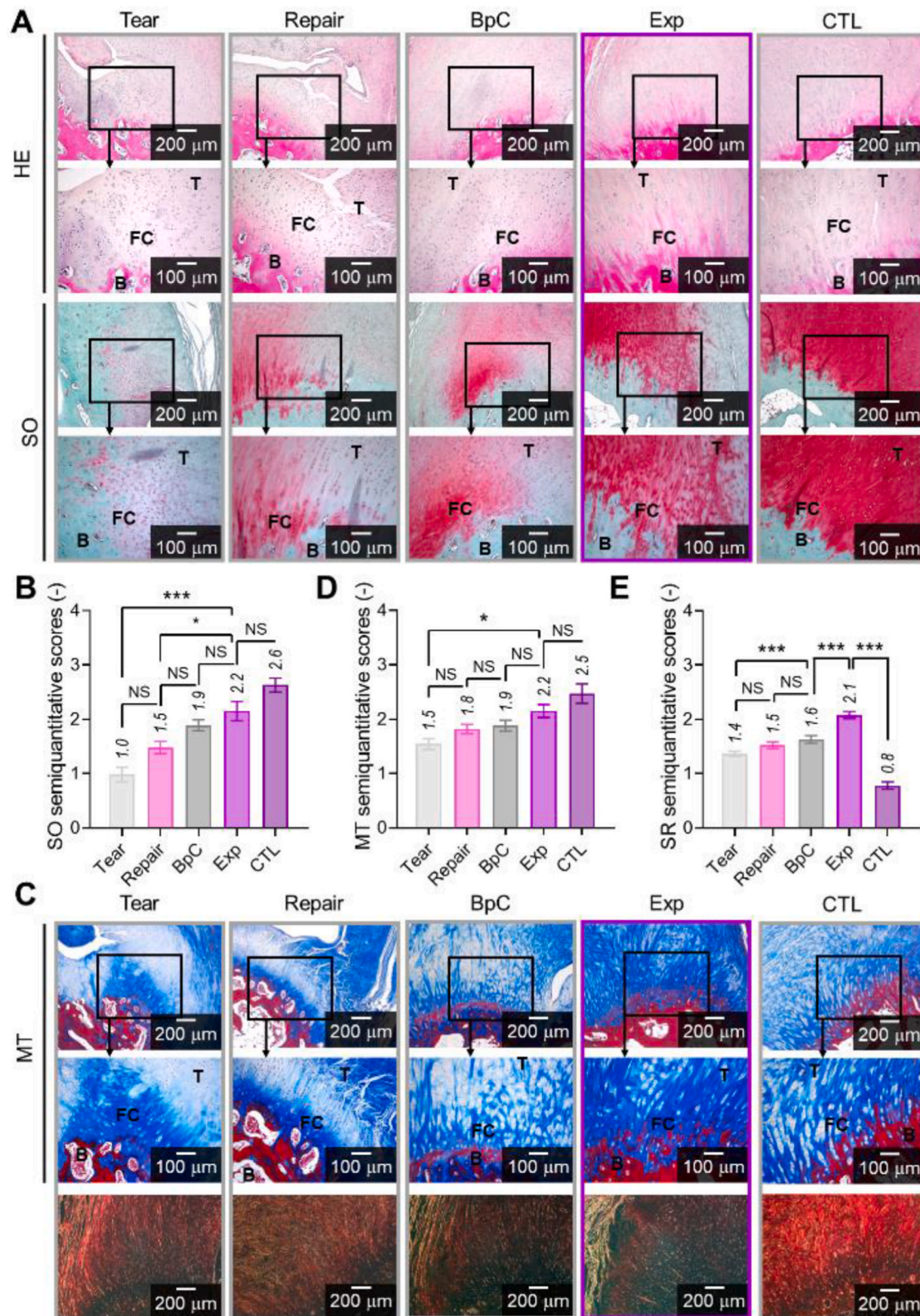


**Fig. 8.** Histological analysis of the biologically graded complex tissue in rabbit rotator cuff tear model. (A) Hematoxylin and eosin (H&E) and Safranin O (SO) staining images of isolated rotator cuff tissue at 8 weeks post-implantation. (B) Semi-quantitatively analyzed SO score (n = 4). (C) Masson's trichrome (MT) and Sirius red (SR) staining images and quantified MT and SR scores 8 weeks post-surgery (n = 4). The black boxes in the upper panels of each group indicate the regions where reconstruction occurred after tissue damage, and these areas are shown at higher magnification in the lower panels. Exp constructs demonstrated the best regenerative capacities by effectively improving the formation of new bone, tendon, and fibrocartilage closely resembling native tissue, resulting in successful regeneration of TBI *in vivo*. All values are presented as the mean  $\pm$  SD (\* $p$  < 0.05, \*\* $p$  < 0.01, and \*\*\* $p$  < 0.001).



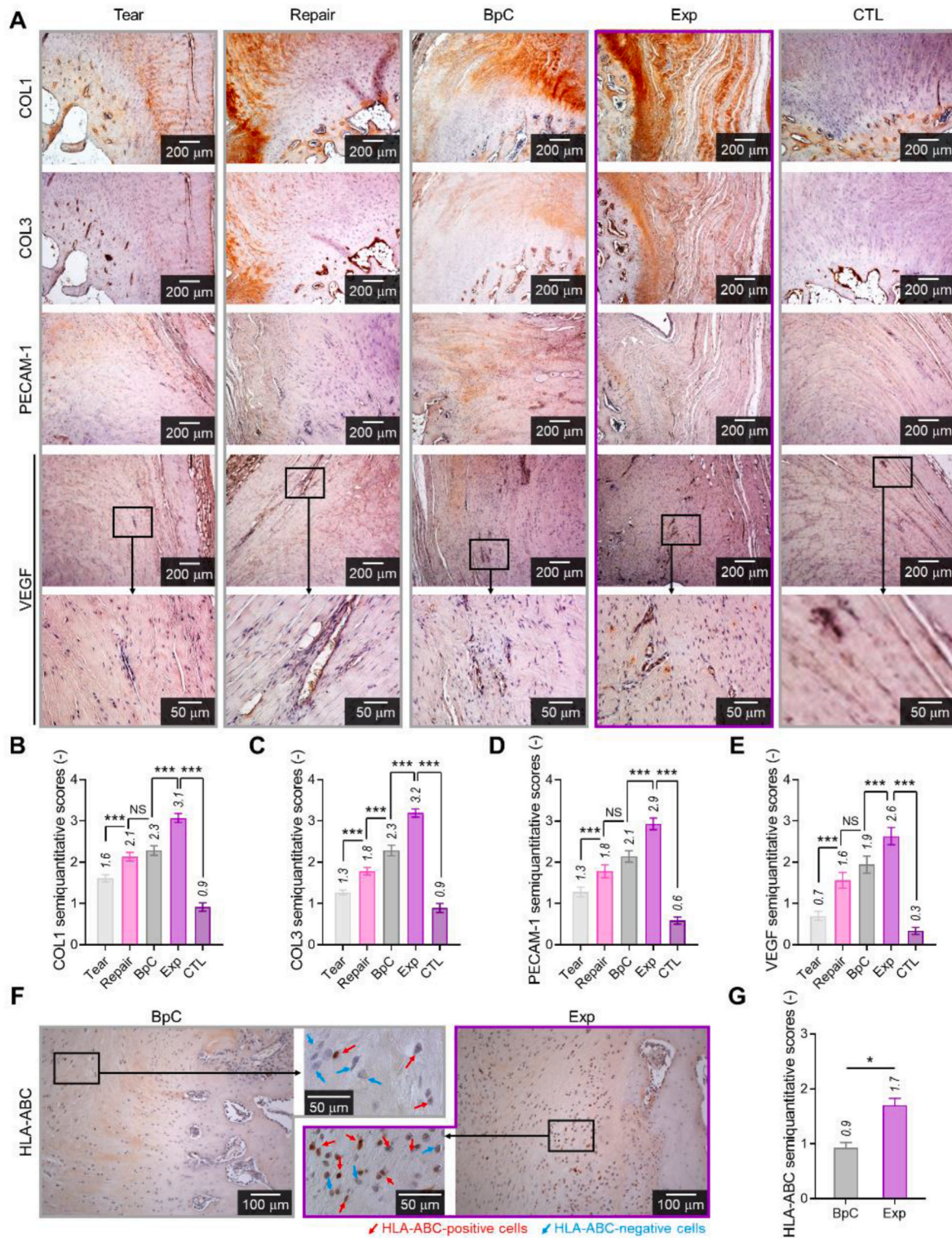


**Fig. 9.** Immunohistochemical imaging of the biprinted TBI construct in rabbit rotator cuff tear model. (A) COL1, COL3, platelet and endothelial cell adhesion molecule 1 (PECAM-1), and vascular endothelial growth factor (VEGF) immunohistochemical staining images at 8 weeks post-implantation. Semi-quantitatively estimated score of (B) COL1, (C) COL3, (D) PECAM-1, and (E) VEGF ( $n = 4$ ). (F) Immunohistochemical staining images and (G) semi-quantitatively analyzed score of HLA Class 1 ABC (HLA-ABC) ( $n = 4$ ). Red and blue arrows indicate the HLA-ABC-positive and -negative cells, respectively. The most efficient regenerative capacities, including tendon-to-bone tissue integration and vascular formation, were observed in the rabbit RCT model with the transplantation of the Exp bioconstructs, validated by immunohistochemical imaging analyses. All values are presented as the mean  $\pm$  SD ( $*p < 0.05$ ,  $**p < 0.01$ , and  $***p < 0.001$ ).

conducted to better elucidate these complexities by performing additional evaluations including the observation of Col2 and Sox9 expressions and observing the regeneration capacities of each tissue separately.

As shown in Fig. 9F—a greater distribution of mouse anti-HLA Class I ABC (HLA-ABC) monoclonal antibody-positive cells near the implantation site, including the newly formed tendon, bone, and fibrocartilage, was observed in the Exp group than in the BpC group (Fig. 9G). This HLA-ABC staining result suggests that the hASCs, which were carried by the bioconstructs, survived well 8 weeks post-operation, and formed tendon-to-bone tissues *in vivo*, with the Exp group demonstrating superior outcomes compared to BpC. Based on the IHC staining results, we concluded that the hASC-loaded soft-to-hard complex construct containing a biologically graded TBI structure efficiently induced angiogenesis and ECM formation, facilitating the restoration of full-thickness tendon-to-bone tissue with a high-quality TBI region and its mechanical function.

In our results, the bioprinted tendon-to-bone tissue with gradient core-shell structures not only demonstrated the efficient formation of the tendon, fibrocartilage, and bone tissues *in vitro*, but also significantly enhanced the remodeling of rotator cuff tissue, resulting in higher quality TBI in an animal model. Although these findings show promising regenerative capacities for RCT repair, several considerations must be addressed to successfully translate this approach into clinical practice. These include ensuring long-term stability and the *in vivo* biodegradation profile to sustain physiological loads [74,75], managing immune responses that could lead to chronic inflammation or fibrous capsule formation [76–78], conducting thorough preclinical and clinical trials in large animal models and human patients, and validating the precise mechanisms underlying hASCs-loaded complex bioconstruct-based tissue regeneration (e.g., hASC differentiation, paracrine signaling, immune modulation, effects of biomaterials, etc. [33,79,80]). With further refinement, we anticipate that the complex tendon-to-bone tissue with a gradient interface, which has demonstrated potential as a strategy to effectively address the limitations of TBI regeneration in current surgical methods, could become a viable alternative for RCT patients in the future.

### 3. Conclusion

In this study, a complex stem cell construct of the tendon-to-bone unit containing a graded TBI structure fabricated by bioprinting, was proposed to integrate torn rotator cuff tissues by replicating the native tissue. Using a core-shell nozzle, porcine tendon- and bone-derived dECM-based bioinks containing hASCs and bioactive factors were bioprinted on each layer of the complex unit. To provide efficient micro-environments for the tenogenesis and osteogenesis of hASCs, bioink-T and bioink-B were prepared by adding cell alignment and tenogenic factors (PVA and TGF- $\beta$ ) and an osteogenic factor (HA) as biological supplements, respectively, based on *in vitro* assessments, including cell viability, alignment, and differentiation. The bioprinted cell constructs using these bioinks exhibited well-differentiated tendon and bone constructs compared with the cell-loaded structures without these factors. For the biologically graded TBI region, both bioinks were bioprinted using a core-shell nozzle to obtain their structures simultaneously. Following the assessment of the fabrication process, two different TBI regions were fabricated to obtain a hierarchical structure. Moreover, each layer of the tendon-to-bone unit was connected by interdigitated boundaries, facilitating the upregulation of fibrocartilage tissue formation compared to the multi-layered structure without interdigitated layers. The resulting complex tissue exhibited significantly improved TBI formation compared with the double-layered tissue without TBI structures, as assessed by immunofluorescence imaging, gene expression analysis, and mechanical tests. In addition, in *in vivo* studies using a rabbit RCT model, the implantation of biologically graded structures facilitated the rapid regeneration of full-thickness tissue with the

formation of a high-quality TBI. The RCT models promoted angiogenesis, ECM formation, and mechanical function restoration after treatment with the graded structure, indicating its potential for clinical use in rotator cuff repair.

## 4. Experimental section

### 4.1. Materials

To formulate bioinks for tendon and bone tissues, porcine-derived bone dECM and photo-crosslinkable tendon dECM were prepared according to previously reported protocols [39,46,81]. In details, porcine-derived bone and tendon tissues were rinsed more than three times with Dulbecco's phosphate-buffered saline (DPBS; Biowest, Nuaille, France) and 3-distilled water (DW). To obtain BdECM, bone power was obtained by crushing and milling the isolated bone tissues, followed by conducting demineralization process by treating 0.5 M HCl for 5 h under continuous stirring at 27 °C. After removing the remaining solution, the remaining lipid r was removed by treating a lipid removal solution consisting of chloroform and methanol for 1 h and then lyophilized in a freeze-drier (SFDSM06; Samwon, Suwon, South Korea) for 3 days. Then, the demineralized bone matrix was decellularized by incubating in trypsin (0.05 %)-ethylenediamine tetra-acetic acid (0.02 %) (TE) solution for 2 h at 37 °C, 70 % ethanol for 1 day, and lyophilized for 3 days. The lyophilized tissue was solubilized by treating pepsin solution (0.1 wt%) dissolved in 0.5 M acetic acid at room temperature for 2 days and precipitated by treating sodium chloride. The digested solution was then dialyzed using 10 kDa molecular cut-off dialysis Tubing (Spectrum Chemical Manufacturing, NJ, USA) at 4 °C for 3 days, followed by lyophilizing the dialyzed solution.

For achieving TdECMA, isolated tendon tissue was cut into small sheets ( $<8 \times 8 \times 1 \text{ mm}^3$ ). Small pieces were decellularized by treating sodium dodecyl sulfate (SDS) solution (1 wt% in DPBS) for 5 days, Triton X-100 (1 % in DPBS) for 2 days, and DNase I solution for 2 h, followed by lyophilizing those for 3 days. Then, the freeze-dried tissues were digested with pepsin solution at room temperature for 2 days, precipitated by treating sodium chloride, centrifuged (3000 rpm) for 15 min, dialyzed for 2 days, and lyophilized for 3 days. The freeze-dried TdECM was stored at  $-80^\circ\text{C}$  before using. To achieve the photo-crosslinkable function, following with dissolving those digested TdECM (3.75 mg/mL) in acetic acid (0.5 M) and adjusting to pH 8–9 using NaOH (1 M) at 4 °C, a methacrylation process was performed by adding methacrylic anhydride at various densities (621 mg per 600 mg of TdECM) under continuous stirring at 4 °C for 2 days. After the chemical modification, the TdECMA solution was dialyzed and freeze-dried. Unless otherwise stated, all chemical reagents were purchased from Sigma-Aldrich. Additionally, the rinsing process with DPBS and DW was performed three times between steps during the decellularization and methacrylation procedures.

In addition, hydroxyapatite (HA) particles, transforming growth factor beta (TGF- $\beta$ ), polyvinyl alcohol (PVA), and Irgacure2959 were purchased from Sigma-Aldrich (St. Louis, MO, USA) to formulate bioinks for tendon and bone tissues. Fibrillated PVA molecules were prepared before formulating the bioinks by dissolving the PVA powder in the DPBS at 95 °C, followed by cooling to room temperature [39].

### 4.2. Bioink preparation

The prepared BdECM and TdECMA were dissolved in an acetic acid solution (1 mM; Sigma-Aldrich), followed by mixing with a  $10 \times$  enriched Dulbecco's modified Eagle's medium (DMEM) solution (Gibco, Waltham, MA, USA) at a ratio of 1:1 to neutralize the solution. Also, human adipose-derived stem cells (hASCs) were purchased from Lonza (Basel, Switzerland) and cultured using DMEM low glucose (DMEM-L; Sigma-Aldrich) supplemented with penicillin/streptomycin (1 %) (PS; Gibco) and fetal bovine serum (10 %) (FBS; Biowest) under a 5 %  $\text{CO}_2$



environment at 37 °C. The medium was changed every two days.

After the preparation of the tissue-derived biomaterials and stem cells, bioink-B and bioink-T were formulated as follows: bioink-B, BdeECM solution was mixed with HA particles (0.2 g/mL) and hASCs ( $2 \times 10^7$  cells/mL) and bioink-T, TdeECMA solution was mixed with TGF- $\beta$  (10 ng/mL), Irgacure2959 (30 mg/mL), PVA (0.1 g/mL), and hASCs ( $2 \times 10^7$  cells/mL). As controls, hASCs ( $2 \times 10^7$  cells/mL)-loaded BdeECM bioink and hASCs ( $2 \times 10^7$  cells/mL)-loaded TdeECMA and TdeECMA/PVA (0.1 g/mL) bioinks were used to evaluate the osteogenic and tenogenic efficacies of bioink-B and bioink-T, respectively. The final concentrations of BdeECM and TdeECMA were 5 wt%. Additionally, BdeECM- and TdeECMA-based bioinks containing diverse concentrations of HA and PVA were used to select the appropriate formulations.

#### 4.3. Bioprinting of tendon-to-bone complex tissue with partially graded TBI

Bioink-B and bioink-T were used to obtain a biomimetic complex construct consisting of graded biological factors using a 3D bioprinting system (DTR3-2210 T-SG; DASA Robot, Bucheon, South Korea) supplemented with a core/shell (bioink-T/bioink-B) nozzle and a pneumatic dispenser (AD-3000C; U-Jin Tech Corp., Seoul, South Korea). The gradient of tenogenesis- and osteogenesis-related biomaterials was achieved by bioprinting both bioinks onto the  $38 \pm 1$  °C working plate with different volume flow rates for each layer. First, the tendon region was fabricated by extruding bioink-T through the core region under UV exposure (300 mW/s<sup>2</sup>) without applying pneumatic pressure to the shell region. Subsequently, the TBI structure consisting of core-shell struts at a volume ratio of 5:5 was bioprinted using both bioinks, and the core-shell structure was fabricated at a ratio of 7.5:2.5. Finally, the bone tissue was obtained by bioprinting bioink-B through the shell region without a core structure. A bioprinted double-layered structure containing tendon and bone tissues without the core-shell structured TBI portion was used as a control. The boundary layer between the two different tissues (tendon-TBI, TBI-TBI, BI-bone, and tendon-bone) was fabricated to include each strut alternately. The conditions of the pneumatic pressure applied to the core and shell regions for each tissue structure are listed in Table 1. The bioprinted complex tissues were cultured using the DMEML-based medium at 37 °C under a 5 % CO<sub>2</sub> environment.

#### 4.4. Characterization of the bioinks and hASCs-constructs

The morphologies of the prepared native tissues, BdeECM, TdeECMA, bioinks, and bioconstructs were captured using an optical microscope (BX FM-32; Olympus, Tokyo, Japan) equipped with a digital camera (Canon, Tokyo Japan) and an SEM (SNE-3000M; SEC Inc., Yeongtong-gu, South Korea). After observing the captured images, ImageJ software (National Institutes of Health, Bethesda, MD, USA) was used to quantitatively analyze the printability, structure thickness, and TdeECMA orientation. All values are exhibited as mean  $\pm$  standard deviation (SD).

Before selecting the formulation of bioink-B and bioink-T, a cone-and-plate geometry (cone angle: 4°, diameter: 40 mm, and gap: 150  $\mu$ m)-attached rotational rheometer (Bohlin Gemini HR Nano; Malvern Instruments, Malvern, UK) was used to assess the rheological properties ( $G'$ , storage modulus and  $\eta^*$ , complex viscosity) of bioinks. Temperature (frequency range: 1 Hz, strain: 1 %, temperature range: 15–45 °C, and ramping rate: 1 °C/min) and frequency (strain: 1 %, temperature: 25 °C, and frequency range: 0.1 Hz–10 Hz) sweeps were applied to the BdeECM-based bioinks consisting of diverse HA compositions and TdeECMA-based bioinks supplemented with different PVA concentrations, respectively. All values are presented as the mean  $\pm$  SD ( $n = 6$ ).

To estimate the mechanical properties of the biomimetic tendon-to-bone tissues, a universal testing machine (SurTA; Chemilab, Suwon, South Korea) was used to stretch the complex hASCs constructs after 3, 14, and 28 days of culture in the wet state under tensile mode (0.1 mm/s of stretching rate). The tendon-to-bone structures were prepared by layering the tendon portion ( $17 \times 6 \times 1.0$  mm<sup>3</sup>), the TBI portion ( $7 \times 6 \times 0.5$  mm<sup>3</sup>), and the bone portion ( $17 \times 6 \times 1.0$  mm<sup>3</sup>) and stretched by fixing the tendon and bone regions. Young's modulus and ultimate tensile strength were estimated using the plotted stress-strain curves. All values are presented as the mean  $\pm$  SD ( $n = 6$ ).

An IRTracer-100 (Shimadzu, Kyoto, Japan) was used to estimate the PVA leaching by comparing the chemical structures of pure dECM, PVA, and dECM/PVA mixtures at the initial state and after 1 day of incubation. The infrared (IR) spectra represent the mean of 30 scans in the range of 650–4000 cm<sup>-1</sup>.

To evaluate the HA contents in each region of the complex tissue, thermogravimetric analysis (TGA) was conducted on the bone, TBI-1, TBI-2, and tendon structures and BpC and Exp tissues using TG/DTA-7300 (SEICO Instruments Inc., Chiba, Japan). The specimens, with a typical mass of 10 mg, were heated from 25 °C to 800 °C (ramp rate: 20 °C/min) under a nitrogen atmosphere.

The *in vitro* biodegradation analysis was evaluated using GM and collagenase solution (0.1 U/mL in DPBS; Sigma-Aldrich). Following the estimation of the initial weight ( $M_i$ ) of the freeze-dried bioconstructs, those were incubated in the GM and collagenase solution for 1, 3, 5, 7, 14, 21, and 28 days at 37 °C under a 5 % CO<sub>2</sub> environment. The specimens were rinsed using DW, lyophilized, and weighed at each time point ( $M_t$ ). The following equation was used to calculate the mass loss:

$$\text{Mass loss} = [(M_i - M_t)/M_i] \times 100$$

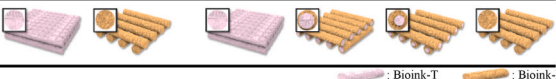
The values of mass loss are shown as the mean  $\pm$  SD ( $n = 6$ ).

#### 4.5. *In vitro* cellular responses and differentiation activities

To visualize the live and dead hASCs, the bioprinted structures were stained by treating with a live/dead staining solution consisting of 0.15 mM calcein AM (Invitrogen, Carlsbad, CA, USA) and 2 mM ethidium homodimer-1 (Invitrogen) for 1 h at 37 °C under 5 % CO<sub>2</sub> environment. After rinsing the stained cells twice with DPBS, they were observed

**Table 1**

**Applied pneumatic pressure.** Conditions of the applied pneumatic pressure to the core and shell regions for each tissue phase of the complex bioconstructs.

	Pneumatic pressure, kPa (Volume flow rate: $\mu$ L/min)					
	BpC		Exp			
	Tendon	Bone	Tendon	TBI-1	TBI-2	Bone
Core (bioink-T)	150 (42)	0 (0)	150 (42)	90 (21)	60 (11)	0 (0)
Shell (bioink-B)	0 (0)	90 (42)	0 (0)	20 (21)	40 (32)	90 (42)
Schematics						



under a confocal microscope (LSM700; Carl Zeiss, Gottingen, Germany). The number of green (live) and red (dead) cells was counted using the ImageJ software to assess cell viability. All values are expressed as mean  $\pm$  SD ( $n = 6$ , six samples per each condition, and five random fields in one sample).

After culturing the bioprinted structures, cellular proliferation was evaluated using a Cell Proliferation Kit I (Boehringer Mannheim, Mannheim, Germany). Following treatment of the cell-loaded structures with MTT solution for 4 h, the metabolically activated hASCs formed purple formazan crystals. To assess cellular proliferation, a sodium dodecyl sulfate (SDS)-based solution was used to dissolve the insoluble crystals, and the optical density (OD) of the purple-colored solution was measured using a microplate spectrophotometer (Epoch; BioTek, Daejeon, South Korea) at 570 nm. All values are presented as mean  $\pm$  SD ( $n = 6$ ).

To confirm cellular morphologies, the nuclei and actin filament were stained with the 4',6-diamidino-2-phenylindole (DAPI) (1:100 in DPBS; Invitrogen) and fluorescein phalloidin (1:100 in DPBS; Invitrogen) staining solution for 1 h. Before incubating with the staining solution, neutral buffered formalin (NBF) (10 % in DPBS; Sigma-Aldrich) and Triton X-100 (2 % in DPBS; Sigma-Aldrich) were treated to fix (for 1 h) and permeabilize (for 10 min) the samples at 37 °C, respectively. The stained cells were visualized using a confocal microscope. ImageJ software was used to quantify cellular alignment and F-actin-positive areas. All values are expressed as means  $\pm$  SD ( $n = 6$ , six samples per each condition, and five random fields in one sample).

After culturing the hASCs loaded in BdeCM-based structures, alkaline phosphatase (ALP) activity was evaluated using an ALP kit (Sigma-Aldrich) to assess the initiation of stem cell osteogenesis. To measure ALP activity, the bioconstructs were incubated with 10 mM Tris-buffer (pH 7.5; Sigma-Aldrich) dissolved in 0.1 % Triton X-100 for 10 min and treated with the lysate containing 100  $\mu$ L of p-nitrophenyl phosphate (p-NPP). The ALP activity was assessed by measuring the amount of p-NPs released p-nitrophenol (p-NP). The absorbances of the samples and known standards were recorded at 450 nm using a microplate reader. Cell-free structures and total protein content were used to normalize the OD values. All values are expressed as means  $\pm$  SD ( $n = 6$ ).

To visualize and evaluate cellular mineralization, ARS staining and calcium deposition assessments were performed on the bone constructs. Before conducting the evaluation process, samples were fixed using 70 % ethanol (Sigma-Aldrich) at 4 °C for 1 h. Then, the fixed cells were incubated with 40 mM ARS solution (pH 4.2; Sigma-Aldrich) or 1 h at room temperature, followed by removal of the remnant ARS components by rinsing the samples thrice using DW. The stained constructs were observed under an optical microscope (Olympus). To estimate calcium deposition, red-colored cells were destained with a 10 % cetylpyridinium chloride (Sigma-Aldrich) solution dissolved in 10 mM sodium phosphate buffer (pH 4.2) for 30 min at room temperature. A microplate spectrophotometer was used to measure the OD of the samples and known standards at 562 nm. Cell-free structures were used to normalize the calcium deposition values. All values are presented as mean  $\pm$  SD ( $n = 6$ ).

To observe the distribution of hASCs loaded in the bioink-B and bioink-T bioprinted using the core-shell nozzle, hASCs were stained with CellTracker™ Red CMTPX Green and CMFDA dyes (Molecular Probes, Eugene, OR, USA) before mixing with bioink-B and bioink-T, respectively. Staining was performed according to the manufacturer's protocol [48]. Following the prewarming of the staining solution, the pre-cultured hASCs were stained with the working solution at 37 °C under a 5 % CO<sub>2</sub> environment for 30 min. Green- and red-stained cells were applied to bioink-T and bioink-B, enabling the visualization of the distribution of bioinks via confocal microscopy.

#### 4.6. Immunofluorescence staining analysis

Before performing the immunofluorescence imaging assessment, the bioprinted samples were fixed (for 1 h), permeabilized (for 2 h), and blocked (for 2 h) at 37 °C using 10 % NBF, 2 % Triton X-100, and 2 % bovine serum albumin (BSA; Sigma-Aldrich), respectively. Then, the prepared cells were incubated with a rabbit anti-collagen type I (COL1) (5  $\mu$ g/mL in DPBS; Invitrogen), a mouse anti-osteopontin (OPN) (5  $\mu$ g/mL in DPBS; Invitrogen), a rabbit anti-tenomodulin (TNMD) (5  $\mu$ g/mL in DPBS; Invitrogen), and a rat anti-aggreacan (ACAN) (5  $\mu$ g/mL in DPBS; Invitrogen) primary antibodies overnight at 4 °C, followed by staining the samples using Alexa Fluor 488- mouse, 594-conjugated rabbit, or 647-conjugated rat secondary antibodies (1:50 in DPBS; Invitrogen) for 1 h at 37 °C. Cellular nuclei were counterstained with DAPI (5  $\mu$ M in DPBS; Invitrogen) solution. After visualizing the stained cells using a confocal microscope (Zeiss), the OPN+, TNMD+, and ACAN + areas were quantified using the ImageJ software. All values are exhibited as mean  $\pm$  SD ( $n = 6$ , six samples per each condition, and five random fields in one sample).

#### 4.7. Polymerase chain reaction-based gene expression analysis

To assess the formation of bone, TBI, and tendon tissues, qRT-PCR analysis was conducted to estimate the expression of osteogenesis, chondrogenesis, and tenogenesis-related genes based on the Livak method (2<sup>− $\Delta\Delta$ CT</sup> method) [82]. First, the cultured cell constructs were treated with TRIzol reagent (Sigma-Aldrich) to isolate total RNA. After treating RNase-free DNase, reverse transcription process was conducted to synthesize cDNA from the RNA using a qPCR RT Master Mix (ReverTraAce™; Toyobo Co., Ltd., Osaka, Japan), followed by performing the qRT-PCR analysis using a qPCR mix (Thunderbird® SYBER®; Toyobo) and a PCR system (StepOnePlus; Applied Biosystems, Foster City, CA, USA). The threshold cycle (CT) values were normalized to the average CT values of the beta-actin (*ACTB*) and glyceraldehyde 3-phosphate dehydrogenase (*GAPDH*) genes in each group. Gene expression results are presented as a comparative fold-change form, defined as the geometric mean and error propagation [82–84]. In addition, the  $\Delta$ CT values (40 cycles) were used to perform statistical analysis. For performing qRT-PCR on an agarose gel (1.2 %), Loading STAR (Dyne Bio, South Korea) was applied to stain the PCR products after 30 cycles, followed by separating those products on the agarose gel using electrophoresis. The primers used are listed in Table S1. All values are reported as mean  $\pm$  SD ( $n = 6$ ).

#### 4.8. Surgical procedures for the development of rabbit RCT

To evaluate the therapeutic potential of the bioprinted tendon-to-bone tissue, a rabbit RCT model was used to perform *in vivo* experiments based on the guidelines approved by the Institutional Animal Care and Use Committee (IACUC) of the Catholic University of Daegu School of Medicine, adhering to the IACUC guidelines for animal care and use (IRB No. DCIAFCR-210304-22-Y). Male New Zealand white rabbits ( $n = 40$ , male, 12 weeks old) with an average weight of 3.3 kg (ranging from 2.8 to 3.6 kg) were obtained from OrientBio Inc. (Gyeonggi, South Korea) and housed individually in steel cages kept at a constant 23  $\pm$  2 °C and under 45  $\pm$  10 % humidity. The animals were provided with tap water and a commercial rabbit diet. After one week of adaptation, the rabbits were randomly divided into four groups ( $n = 8$  per group). Rabbits were anesthetized with isoflurane (Forane; JW Pharmaceutical Corp., Seoul, South Korea). A full-thickness partial-width rotator cuff tear (FTPWRCT) of 5 (diameter)  $\times$  5 (depth) mm<sup>3</sup> was created at the bone-tendon interface of the right supraspinatus tendon. To model chronic FTPWRCT, the excision site was immediately covered with a nonabsorbable round silicone Penrose drainage tube (Sewoon Medical Co., Ltd.) as described in prior studies [85–91]. Sutures were placed on the subcutaneous tissue and skin to close the incisions. Six weeks after

the FTPWRCT, the Penrose drainage tube was removed, and the status of the chronic FTPWRCT was observed. Our study involved a total of 40 rabbits, which were randomly divided into five groups. The groups included: no implants without self-repair (Tear), self-repair without implants (Repair), implantation of BpC and Exp constructs, and rabbits without RCT, which served as controls (CTL). A suture was then threaded through the torn tendon, passed through the drilled bone tunnel, and secured to reattach the tendon to its original site on the greater tuberosity. The sutured tendon was attached to the implanted TBI structures, and the opposite end of the suture was anchored to the humerus using 3-0 nylon. This suture technique was performed on the Repair, BpC, and Exp groups.

Each of the four experimental groups consisted of eight rabbits ( $n = 8$  per group), totaling 32 animals. An additional eight rabbits were included as controls, bringing the overall total to 40 animals. For histological analysis, the right supraspinatus of four rabbits in each group was immersed in a 4 % paraformaldehyde solution. The right supraspinatus of the remaining four rabbits in each group was dissected for biomechanical testing shortly after dissection.

In the Tear group (no implants without self-repair), the RCT was created, but no interventions were applied to promote healing, meaning the tendon was left untreated. In the Repair group (self-repair without implants), the RCT was created, and the tendon was surgically reattached without using any implants, allowing for natural healing and repair. In the implantation groups, after creating the RCT, specific experimental constructs (BpC and Exp) sized to the defect were implanted at the repair site, the torn tendon tissue was reattached with sutures. In the study, the bioprinted biomimetic complex tissues with (Exp) and without (BpC) biologically graded TBI structures (Fig. 7A).

#### 4.9. Biomechanical analysis

Eight weeks post-operation, the biomechanical properties of the restored tendon-to-bone tissue were evaluated using the SurTA universal testing machine in tensile mode based on previously reported methods, with isolated tissues from five animals [12]. The proximal humeral head and supraspinatus tendon of the complex tissues obtained from the CTL, Tear, Repair, BpC, and Exp groups were fixed along the longitudinal axis of the tendon fibers, allowing the loads to be applied along the anatomical direction at the manipulated stretching rate (0.1 mm/s). The maximum load and stiffness (slope of the linear region [26]) were estimated using the plotted load-distance curves. Values are presented as the representative results for the load-distance curves and the mean  $\pm$  SD for the estimated maximum load and stiffness ( $n = 4$ ).

#### 4.10. Imaging analysis for in vivo evaluation

Specimens were fixed immediately after euthanasia and subsequently stained with Hematoxylin and Eosin (H&E), Masson-Trichrome (MT), Safranin O, and Sirius Red. To examine collagen distribution and angiogenesis at the site of regeneration, immunohistochemical techniques using antibodies specific to collagen type 1, collagen type 3, platelet endothelial cell adhesion molecule 1, and vascular endothelial growth factor were applied.

For immunohistochemical staining, paraffin-embedded sections were cleared, dehydrated, and washed with PBS. For antigen retrieval, the sections were incubated in citrate buffer (pH 6.0) for 30 min at 95 °C. After incubation, the endogenous peroxidases were blocked with 0.3 % hydrogen peroxide in PBS for 30 min. Non-specific antibody binding was blocked in PBS containing 10 % normal horse, goat, or rabbit serum (Vector Laboratories, Newark, CA, USA) for 30 min. The sections were washed three times with PBS and incubated with primary antibodies (1:100–1:200) at room temperature for 2 h. The following primary antibodies were used: mouse anti-collagen 1 (COL1) monoclonal antibody (Abcam, Waltham, MA, USA), mouse anti-collagen 3 (COL3) monoclonal antibody (FH-7A; Abcam), goat anti-platelet endothelial cell

adhesion molecule 1 (PECAM-1) polyclonal antibody (M-20; Santa Cruz Biotechnology, Santa Cruz, CA, USA), rabbit anti-VEGF polyclonal antibody (A-20; Santa Cruz Biotechnology), and mouse anti-HLA Class 1 ABC (HLA-ABC; reactivity: human) monoclonal antibody (EMR8-5; Abcam). Subsequently, sections were incubated with the following secondary antibodies (1:100) at room temperature for 1 h: biotinylated anti-mouse immunoglobulin G (IgG), biotinylated anti-goat IgG, and biotinylated anti-rabbit IgG (Vector Laboratories). The sections were washed with PBS three times and treated with avidin-biotin-peroxidase complex (Vector Laboratories) for 1 h, washed again in PBS three times, and subjected to peroxidase reaction with 0.05 M Tris-HCl (pH 7.6) containing 0.01 % hydrogen peroxide and 0.05 % 3,3'-diaminobenzidine (Sigma-Aldrich). Counterstaining was performed using hematoxylin.

An Axiophot Photomicroscope and an AxioCam MRC5 (Zeiss) were used for examination of the prepared sections and image storage. An AxioVision SE64 (Zeiss) was used to analyze the stored images. Eight fields of view were randomly selected and photographed on each slide. As secondary outcome measures, the intensity and extent of positive immunostaining were evaluated and converted to semi-quantitative scores of 0–4. Masson's trichrome, SO, and SR staining intensities and COL1, COL3, PECAM-1, and VEGF immunostaining intensities were scored as 0 (negative staining), 1 (weak staining but detectable), 2 (mildly positive staining), 3 (moderately positive staining), or 4 (strongly positive staining). For HLA-ABC, the proportion of positively stained cells was evaluated and scored as 0 (no positively stained cells), 1 (1%–10 % positive-stained cells), 2 (11%–33 %), 3 (34%–66 %), and 4 (67%–100 %). All values are presented as the mean  $\pm$  SD ( $n = 4$ , four samples per each condition, and five random fields in one sample). To minimize subjectivity, five fields were randomly selected and photographed from each section for semiquantitative analysis. The scoring was performed twice on separate occasions by two independent researchers who were blinded to group allocation: one with more than 20 years of experience as an anatomist (Rater 1) and a trained researcher (Rater 2). Weighted Kappa was used to assess the intra- and inter-observer reliability of the semiquantitative scoring. Intra-rater reliability was calculated at 0.865, indicating strong agreement, while inter-rater reliability was 0.778, indicating substantial agreement.

#### 4.11. Statistical analysis

Statistical analyses were performed using the SPSS software (SPSS, Inc., Chicago, IL, USA) with Student's t-test and analysis of variance (ANOVA) supplemented with Tukey's honest significant difference (HSD) post-hoc test for comparisons between two groups and three or more groups. Values of  $*p < 0.05$ ,  $**p < 0.01$ , and  $***p < 0.001$  were considered statistically significant.

#### Ethics approval and consent to participate

All the protocols for animal experiments were approved by the Institutional Animal Care and Use Committee of the Catholic University of Daegu School of Medicine (IRB No. DCIAFCR-210304-22-Y) and conducted according to their recommended guidelines.

#### Data availability

The data in this work are available in the manuscript or Supplementary Information, or available from the corresponding author upon reasonable request.

#### CRediT authorship contribution statement

**WonJin Kim:** Writing – original draft, Formal analysis, Data curation, Conceptualization. **Dong Rak Kwon:** Writing – original draft, Formal analysis, Data curation. **Hyeongjin Lee:** Writing – original draft, Formal analysis, Data curation. **JaeYoon Lee:** Formal analysis. **Yong**



**Suk Moon:** Formal analysis. **Sang Chul Lee:** Writing – review & editing, Supervision. **Geun Hyung Kim:** Writing – review & editing, Writing – original draft, Supervision, Methodology, Investigation, Conceptualization.

### Declaration of competing interest

The authors declare that they have no known competing financial interests or personal relationships that could have appeared to influence the work reported in this paper.

### Acknowledgments

This research was supported by the “Korea National Institute of Health” research project (2022ER130500) and grants from the National Research Foundation of Korea (NRF) funded by the Korea government (MSIT) (RS-2024-00336758), (No. NRF2022R1F1A106729811) and (2022R1A2C2091162). This research was also supported by the Sung-KyunKwan University and the BK21 FOUR (Graduate School Innovation) funded by the Ministry of Education (MOE, Korea) and National Research Foundation of Korea (NRF).

### Appendix A. Supplementary data

Supplementary data to this article can be found online at <https://doi.org/10.1016/j.bioactmat.2024.10.002>.

### References

- [1] H. Ramakrishna, T. Li, T. He, J. Temple, M.W. King, A. Spagnoli, Tissue engineering a tendon-bone junction with biodegradable braided scaffolds, *Biomater. Res.* 23 (1) (2019) 11.
- [2] D. Wang, X. Zhang, S. Huang, Y. Liu, B.S.-c. Fu, K.K.-l. Mak, A.M. Blocki, P.S.-h. Yung, R.S. Tuan, Engineering multi-tissue units for regenerative medicine: bone-tendon-muscle units of the rotator cuff, *Biomaterials* 272 (2021) 120789.
- [3] T. Lei, T. Zhang, W. Ju, X. Chen, B.C. Heng, W. Shen, Z. Yin, Biomimetic strategies for tendon/ligament-to-bone interface regeneration, *Bioact. Mater.* 6 (8) (2021) 2491–2510.
- [4] G.P. Dang, W. Qin, Q.Q. Wan, J.T. Gu, K.Y. Wang, Z. Mu, B. Gao, K. Jiao, F.R. Tay, L.N. Niu, Regulation and reconstruction of cell phenotype gradients along the tendon-muscle interface, *Adv. Funct. Mater.* 33 (2) (2023) 2210275.
- [5] C. Niyibizi, C.S. Visconti, G. Gibson, K. Kavalkovich, Identification and immunolocalization of type X collagen at the ligament–bone interface, *Biochem. Biophys. Res. Commun.* 222 (2) (1996) 584–589.
- [6] L.M. Galatz, C.M. Ball, S.A. Teefey, W.D. Middleton, K. Yamaguchi, The outcome and repair integrity of completely arthroscopically repaired large and massive rotator cuff tears, *J. Bone Joint Surg.* 86 (2) (2004) 219–224.
- [7] K.A. Derwin, L.M. Galatz, A. Ratcliffe, S. Thomopoulos, Enthesis repair: challenges and opportunities for effective tendon-to-bone healing, *J. Bone Joint Surg.* 100 (16) (2018) e109.
- [8] S. Thomopoulos, G. Williams, L. Soslowsky, Tendon to bone healing: differences in biomechanical, structural, and compositional properties due to a range of activity levels, *J. Biol. Chem.* 125 (1) (2003) 106–113.
- [9] S.A. Rodeo, S.P. Arnoczky, P.A. Torzilli, C. Hidaka, R.F. Warren, Tendon-healing in a bone tunnel. A biomechanical and histological study in the dog, *J. Bone Joint Surg.* 75 (12) (1993) 1795–1803.
- [10] R. Newsham-West, H. Nicholson, M. Walton, P. Milburn, Long-term morphology of a healing bone–tendon interface: a histological observation in the sheep model, *J. Anat.* 210 (3) (2007) 318–327.
- [11] L. Du, C. Qin, H. Zhang, F. Han, J. Xue, Y. Wang, J. Wu, Y. Xiao, Z. Huan, C. Wu, Multicellular bioprinting of biomimetic inks for tendon-to-bone regeneration, *Adv. Sci.* 10 (21) (2023) 2301309.
- [12] X. Jiang, Y. Kong, M. Kuss, J. Weisenburger, H. Haider, R. Harms, W. Shi, B. Liu, W. Xue, J. Dong, 3D bioprinting of multilayered scaffolds with spatially differentiated ADMSCs for rotator cuff tendon-to-bone interface regeneration, *Appl. Mater. Today* 27 (2022) 101510.
- [13] Z. Mao, B. Fan, X. Wang, X. Huang, J. Guan, Z. Sun, B. Xu, M. Yang, Z. Chen, D. Jiang, A systematic review of tissue engineering scaffold in tendon bone healing in vivo, *Front. Bioeng. Biotechnol.* 9 (2021) 621483.
- [14] S. Chae, Y. Sun, Y.-J. Choi, D.-H. Ha, I. Jeon, D.-W. Cho, 3D cell-printing of tendon-bone interface using tissue-derived extracellular matrix bioinks for chronic rotator cuff repair, *Biofabrication* 13 (3) (2021) 035005.
- [15] S. Chae, D.-W. Cho, Biomaterial-based 3D bioprinting strategy for orthopedic tissue engineering, *Acta Biomater.* 156 (2023) 4–20.
- [16] S. Park, K.A. Rahaman, Y.-C. Kim, H. Jeon, H.-S. Han, Fostering tissue engineering and regenerative medicine to treat musculoskeletal disorders in bone and muscle, *Bioact. Mater.* 40 (2024) 345–365.
- [17] X. Cui, J. Li, Y. Hartanto, M. Durham, J. Tang, H. Zhang, G. Hooper, K. Lim, T. Woodfield, Advances in extrusion 3D bioprinting: a focus on multicomponent hydrogel-based bioinks, *Adv. Healthcare Mater.* 9 (15) (2020) 1901648.
- [18] L. Ning, C.J. Gil, B. Hwang, A.S. Theus, L. Perez, M.L. Tomov, H. Bauser-Heaton, V. Serpooshan, Biomechanical factors in three-dimensional tissue bioprinting, *Appl. Phys. Rev.* 7 (4) (2020).
- [19] D. Choudhury, H.W. Tun, T. Wang, M.W. Naing, Organ-derived decellularized extracellular matrix: a game changer for bioink manufacturing? *Trends Biotechnol.* 36 (8) (2018) 787–805.
- [20] B.S. Kim, S. Das, J. Jang, D.-W. Cho, Decellularized extracellular matrix-based bioinks for engineering tissue-and organ-specific microenvironments, *Chem. Rev.* 120 (19) (2020) 10608–10661.
- [21] W. Park, G. Gao, D.-W. Cho, Tissue-specific decellularized extracellular matrix bioinks for musculoskeletal tissue regeneration and modeling using 3D bioprinting technology, *Int. J. Mol. Sci.* 22 (15) (2021) 7837.
- [22] H. Hwangbo, J. Lee, G. Kim, Mechanically and biologically enhanced 3D-printed HA/PLLA/dECM biocomposites for bone tissue engineering, *Int. J. Biol. Macromol.* 218 (2022) 9–21.
- [23] C. Yang, Y. Teng, B. Geng, H. Xiao, C. Chen, R. Chen, F. Yang, Y. Xia, Strategies for promoting tendon-bone healing: current status and prospects, *Front. Bioeng. Biotechnol.* 11 (2023) 1118468.
- [24] L. Du, J. Wu, Y. Han, C. Wu, Immunomodulatory multicellular scaffolds for tendon-to-bone regeneration, *Sci. Adv.* 10 (10) (2024) eadk6610.
- [25] L. Bai, Q. Han, Z. Meng, B. Chen, X. Qu, M. Xu, Y. Su, Z. Qiu, Y. Xue, J. He, Bioprinted living tissue constructs with layer-specific, growth factor-loaded microspheres for improved enthesis healing of a rotator cuff, *Acta Biomater.* 154 (2022) 275–289.
- [26] S. Chae, U. Yong, W. Park, Y.-m. Choi, I.-H. Jeon, H. Kang, J. Jang, H.S. Choi, D.-W. Cho, 3D cell-printing of gradient multi-tissue interfaces for rotator cuff regeneration, *Bioact. Mater.* 19 (2023) 611–625.
- [27] X. Zhang, W. Song, K. Han, Z. Fang, E. Cho, X. Huangfu, Y. He, J. Zhao, Three-dimensional bioprinting of a structure-, composition-, and mechanics-graded biomimetic scaffold coated with specific decellularized extracellular matrix to improve the tendon-to-bone healing, *ACS Appl. Mater. Interfaces* 15 (24) (2023) 28964–28980.
- [28] Y. Qin, G. Ge, P. Yang, L. Wang, Y. Qiao, G. Pan, H. Yang, J. Bai, W. Cui, D. Geng, An update on adipose-derived stem cells for regenerative medicine: where challenge meets opportunity, *Adv. Sci.* 10 (20) (2023) 2207334.
- [29] J. Wang, S. Su, C. Dong, Q. Fan, J. Sun, S. Liang, Z. Qin, C. Ma, J. Jin, H. Zhu, Human adipose-derived stem cells upregulate IGF-1 and alleviate osteoarthritis in a two-stage rabbit osteoarthritis model, *Curr. Stem Cell Res. Ther.* 19 (11) (2024) 1472–1483.
- [30] Y.-z. Zhu, X. Hu, J. Zhang, Z.-h. Wang, S. Wu, Y.-y. Yi, Extracellular vesicles derived from human adipose-derived stem cell prevent the formation of hypertrophic scar in a rabbit model, *Ann. Plast. Surg.* 84 (5) (2020) 602–607.
- [31] J. Lasso, R.P. Cano, Y. Castro, L. Arenas, J. García, M. Fernández-Santos, Xenotransplantation of human adipose-derived stem cells in the regeneration of a rabbit peripheral nerve, *J. Plast. Reconstr. Aesthetic Surg.* 68 (12) (2015) e189–e197.
- [32] G.-Y. Park, D.R. Kwon, S.C. Lee, Regeneration of full-thickness rotator cuff tendon tear after ultrasound-guided injection with umbilical cord blood-derived mesenchymal stem cells in a rabbit model, *Stem Cells Transl. Med.* 4 (11) (2015) 1344–1351.
- [33] F. Mocini, A.S. Monteleone, P. Piazza, V. Cardona, V. Vismara, P. Messinese, V. Campana, G. Sircana, G. Maccauro, M.F. Saccomanno, The role of adipose derived stem cells in the treatment of rotator cuff tears: from basic science to clinical application, *Orthop. Rev.* 12 (Suppl 1) (2020).
- [34] W. Duan, M. Haque, M.T. Kearney, M.J. Lopez, Collagen and hydroxyapatite scaffolds activate distinct osteogenesis signaling pathways in adult adipose-derived multipotent stromal cells, *Tissue Eng. C Methods* 23 (10) (2017) 592–603.
- [35] C. Zhao, X. Wang, L. Gao, L. Jing, Q. Zhou, J. Chang, The role of the micro-pattern and nano-topography of hydroxyapatite bioceramics on stimulating osteogenic differentiation of mesenchymal stem cells, *Acta Biomater.* 73 (2018) 509–521.
- [36] W. Kim, G. Kim, Collagen/bioceramic-based composite bioink to fabricate a porous 3D hASCs-laden structure for bone tissue regeneration, *Biofabrication* 12 (1) (2019) 015007.
- [37] D.A. Kaji, K.L. Howell, Z. Balic, D. Hubmacher, A.H. Huang, Tgfb signaling is required for tenocyte recruitment and functional neonatal tendon regeneration, *Elife* 9 (2020) e51779.
- [38] G. Yang, B. Rothrauff, H. Lin, R. Gottardi, R. Tuan, Tendon-derived Extracellular Matrix Enhances TGF-Beta 3 Induced Tenogenic Differentiation of Human Adipose-Derived Stem Cells, 2014, pp. S24–S25. *Tissue Eng. Part A*, MARY ANN LIEBERT, INC 140 HUGUENOT STREET, 3RD FL, NEW ROCHELLE, NY 10801 USA.
- [39] W. Kim, H. Lee, J. Lee, A. Atala, J.J. Yoo, S.J. Lee, G.H. Kim, Efficient myotube formation in 3D bioprinted tissue construct by biochemical and topographical cues, *Biomaterials* 230 (2020) 119632.
- [40] H. Lee, W. Kim, J. Lee, K.S. Park, J.J. Yoo, A. Atala, G.H. Kim, S.J. Lee, Self-aligned myofibers in 3D bioprinted extracellular matrix-based construct accelerate skeletal muscle function restoration, *Appl. Phys. Rev.* 8 (2) (2021) 021405.
- [41] W. Kim, M. Kim, G.H. Kim, 3D-printed biomimetic scaffold simulating microfibril muscle structure, *Adv. Funct. Mater.* 28 (26) (2018) 1800405.
- [42] Y.W. Koo, G.H. Kim, Bioprinted hASC-laden collagen/HA constructs with meringue-like macro/micro pores, *Bioeng. Transl. Med.* (2022) e10330.
- [43] J. Xing, N. Liu, N. Xu, W. Chen, D. Xing, Engineering complex anisotropic scaffolds beyond simply uniaxial alignment for tissue engineering, *Adv. Funct. Mater.* 32 (15) (2022) 2110676.

- [44] B.S. Heidari, R. Ruan, E. Vahabli, P. Chen, E.M. De-Juan-Pardo, M. Zheng, B. Doyle, Natural, synthetic and commercially-available biopolymers used to regenerate tendons and ligaments, *Bioact. Mater.* 19 (2023) 179–197.
- [45] G. Yang, B.B. Rothrauff, H. Lin, R. Gottardi, P.G. Alexander, R.S. Tuan, Enhancement of tenogenic differentiation of human adipose stem cells by tendon-derived extracellular matrix, *Biomaterials* 34 (37) (2013) 9295–9306.
- [46] J. Lee, J. Hong, W. Kim, G.H. Kim, Bone-derived ECM/alginate bioink for fabricating a 3D cell-laden mesh structure for bone tissue engineering, *Carbohydr. Polym.* 250 (2020) 116914.
- [47] W. Kim, C.H. Jang, G. Kim, Bone tissue engineering supported by bioprinted cell constructs with endothelial cell spheroids, *Theranostics* 12 (12) (2022) 5404.
- [48] W. Kim, H. Lee, E.J. Roh, S.B. An, I.-B. Han, G.H. Kim, A multicellular bioprinted cell construct for vascularized bone tissue regeneration, *Chem. Eng. J.* 431 (2022) 133882.
- [49] S.M. Hull, L.G. Brunel, S.C. Heilshorn, 3D bioprinting of cell-laden hydrogels for improved biological functionality, *Adv. Mater.* 34 (2) (2022) 2103691.
- [50] D. Kim, H. Lee, G.H. Lee, T.H. Hoang, H.R. Kim, G.H. Kim, Fabrication of bone-derived decellularized extracellular matrix/Ceramic-based biocomposites and their osteo/odontogenic differentiation ability for dentin regeneration, *Bioeng. Transl. Med.* (2022) e10317.
- [51] L. Ouyang, R. Yao, Y. Zhao, W. Sun, Effect of bioink properties on printability and cell viability for 3D bioplotting of embryonic stem cells, *Biofabrication* 8 (3) (2016) 035020.
- [52] C. Liu, P. Wan, L.L. Tan, K. Wang, K. Yang, Preclinical investigation of an innovative magnesium-based bone graft substitute for potential orthopaedic applications, *J. Orthop. Translat.* 2 (3) (2014) 139–148.
- [53] C. Kolf, E. Cho, R. Tuan, Biology of Adult Mesenchymal Stem Cells: Regulation of Niche, Self-Renewal and Differentiation, 2007.
- [54] M. Wu, G. Chen, Y.-P. Li, TGF- $\beta$  and BMP signaling in osteoblast, skeletal development, and bone formation, homeostasis and disease, *Bone Res* 4 (1) (2016) 1–21.
- [55] J.M. Sadowska, J. Guillem-Marti, M. Espanol, C. Stähli, N. Döbelin, M.-P. Ginebra, In vitro response of mesenchymal stem cells to biomimetic hydroxyapatite substrates: a new strategy to assess the effect of ion exchange, *Acta Biomater.* 76 (2018) 319–332.
- [56] A.M. Yadav, M.M. Bagade, S. Ghumnani, S. Raman, B. Saha, K.F. Kubatzky, R. Ashma, The phytochemical plumbagin reciprocally modulates osteoblasts and osteoclasts, *Biol. Chem.* 403 (2) (2022) 211–229.
- [57] S.J. Roberts, Y. Chen, M. Moesen, J. Schrooten, F.P. Luyten, Enhancement of osteogenic gene expression for the differentiation of human periosteal derived cells, *Stem Cell Res.* 7 (2) (2011) 137–144.
- [58] K. Li, X. Zhang, D. Wang, R.S. Tuan, Synergistic effects of growth factor-based serum-free medium and tendon-like substrate topography on tenogenesis of mesenchymal stem cells, *Biomater. Adv.* 146 (2023) 213316.
- [59] Y. Yoshimoto, A. Uezumi, M. Ikemoto-Uezumi, K. Tanaka, X. Yu, T. Kurosawa, S. Yambe, K. Maehara, Y. Ohkawa, Y. Sotomaru, Tenogenic induction from induced pluripotent stem cells unveils the trajectory towards tenocyte differentiation, *Front. Cell Dev. Biol.* 10 (2022) 780038.
- [60] V. Kishore, W. Bullock, X. Sun, W.S. Van Dyke, O. Akkus, Tenogenic differentiation of human MSCs induced by the topography of electrochemically aligned collagen threads, *Biomaterials* 33 (7) (2012) 2137–2144.
- [61] W.J. Kim, G.H. Kim, A bioprinted complex tissue model for myotendinous junction with biochemical and biophysical cues, *Bioeng. Transl. Med.* (2022) e10321.
- [62] I.M. Jipa, A. Stoica, M. Stroescu, L.-M. Dobre, T. Dobre, S. Jinga, C. Tardei, Potassium sorbate release from poly (vinyl alcohol)-bacterial cellulose films, *Chem. Pap.* 66 (2012) 138–143.
- [63] S.M. Wahl, N. McCartney-Francis, S.E. Mergenhagen, Inflammatory and immunomodulatory roles of TGF- $\beta$ , *Immunol. Today* 10 (8) (1989) 258–261.
- [64] A. Moustakas, K. Pardali, A. Gaal, C.-H. Heldin, Mechanisms of TGF- $\beta$  signaling in regulation of cell growth and differentiation, *Immunol. Lett.* 82 (1–2) (2002) 85–91.
- [65] Y. Li, X. Liu, X. Liu, Y. Peng, B. Zhu, S. Guo, C. Wang, D. Wang, S. Li, Transforming growth factor- $\beta$  signalling pathway in tendon healing, *Growth Factors* 40 (3–4) (2022) 98–107.
- [66] I. Donderwinkel, R.S. Tuan, N.R. Cameron, J.E. Frith, Tendon tissue engineering: current progress towards an optimized tenogenic differentiation protocol for human stem cells, *Acta Biomater.* 145 (2022) 25–42.
- [67] R. Yang, G. Li, C. Zhuang, P. Yu, T. Ye, Y. Zhang, P. Shang, J. Huang, M. Cai, L. Wang, Gradient bimetallic ion-based hydrogels for tissue microstructure reconstruction of tendon-to-bone insertion, *Sci. Adv.* 7 (26) (2021) eabg3816.
- [68] Y. Cao, S. Yang, D. Zhao, Y. Li, S.S. Cheong, D. Han, Q. Li, Three-dimensional printed multiphasic scaffolds with stratified cell-laden gelatin methacrylate hydrogels for biomimetic tendon-to-bone interface engineering, *J. Orthop. Translat.* 23 (2020) 89–100.
- [69] S.F. Tellado, E.R. Balmayor, M. Van Griensven, Strategies to engineer tendon/ligament-to-bone interface: biomaterials, cells and growth factors, *Adv. Drug Deliv. Rev.* 94 (2015) 126–140.
- [70] S. Zhou, S. Chen, Q. Jiang, M. Pei, Determinants of stem cell lineage differentiation toward chondrogenesis versus adipogenesis, *Cell. Mol. Life Sci.* 76 (2019) 1653–1680.
- [71] M. Zhao, X. Gao, J. Wei, C. Tu, H. Zheng, K. Jing, J. Chu, W. Ye, T. Groth, Chondrogenic differentiation of mesenchymal stem cells through cartilage matrix-inspired surface coatings, *Front. Bioeng. Biotechnol.* 10 (2022) 991855.
- [72] J.R. Merkel, B.R. DiPaolo, G.G. Hallock, D.C. Rice, Type I and type III collagen content of healing wounds in fetal and adult rats, *Proc. Soc. Exp. Biol. Med.* 187 (4) (1988) 493–497.
- [73] S.W. Volk, Y. Wang, E.A. Mauldin, K.W. Liechty, S.L. Adams, Diminished type III collagen promotes myofibroblast differentiation and increases scar deposition in cutaneous wound healing, *Cells Tissues Organs* 194 (1) (2011) 25–37.
- [74] X. Zhang, D. Wang, Z. Wang, S.K.-k. Ling, P.S.-h. Yung, R.S. Tuan, Clinical perspectives for repairing rotator cuff injuries with multi-tissue regenerative approaches, *J. Orthop. Translat.* 36 (2022) 91–108.
- [75] J. Chen, J. Xu, A. Wang, M. Zheng, Scaffolds for tendon and ligament repair: review of the efficacy of commercial products, *Expert Rev. Med. Dev.* 6 (1) (2009) 61–73.
- [76] S.F. Badylak, T.W. Gilbert, Immune response to biologic scaffold materials. *Seminars in Immunology*, Elsevier, 2008, pp. 109–116.
- [77] B.N. Brown, J.E. Valentin, A.M. Stewart-Akers, G.P. McCabe, S.F. Badylak, Macrophage phenotype and remodeling outcomes in response to biologic scaffolds with and without a cellular component, *Biomaterials* 30 (8) (2009) 1482–1491.
- [78] T.J. Keane, I.T. Swinehart, S.F. Badylak, Methods of tissue decellularization used for preparation of biologic scaffolds and in vivo relevance, *Methods* 84 (2015) 25–34.
- [79] R. Whitaker, B. Hernaez-Estrada, R.M. Hernandez, E. Santos-Vizcaino, K.L. Spiller, Immunomodulatory biomaterials for tissue repair, *Chem. Rev.* 121 (18) (2021) 11305–11335.
- [80] A.K. Gaharwar, I. Singh, A. Khademhosseini, Engineered biomaterials for in situ tissue regeneration, *Nat. Rev. Mater.* 5 (9) (2020) 686–705.
- [81] Y. Rao, C. Zhu, H.C. Suen, S. Huang, J. Liao, D.F.E. Ker, R.S. Tuan, D. Wang, Tenogenic induction of human adipose-derived stem cells by soluble tendon extracellular matrix: composition and transcriptomic analyses, *Curr. Stem Cell Res. Ther.* 13 (1) (2022) 380.
- [82] K.J. Livak, T.D. Schmittgen, Analysis of relative gene expression data using real-time quantitative PCR and the 2- $\Delta\Delta CT$  method, *Methods* 25 (4) (2001) 402–408.
- [83] S.A. Bustin, V. Benes, J.A. Garson, J. Hellemans, J. Huggett, M. Kubista, R. Mueller, T. Nolan, M.W. Pfaffl, G.L. Shipley, The MIQE Guidelines: Minimum Information for Publication of Quantitative Real-Time PCR Experiments, Oxford University Press, 2009.
- [84] J. Vandesompele, K. De Preter, F. Pattyn, B. Poppe, N. Van Roy, A. De Paepe, F. Speleman, Accurate normalization of real-time quantitative RT-PCR data by geometric averaging of multiple internal control genes, *Genome Biol.* 3 (7) (2002) 1–12.
- [85] S.H. Coleman, S. Fealy, J.R. Ehteshami, J.D. MacGillivray, D.W. Altchek, R. F. Warren, A.S. Turner, Chronic rotator cuff injury and repair model in sheep, *J. Bone Joint Surg.* 85 (12) (2003) 2391–2402.
- [86] D.R. Kwon, K.L. Kim, Y.S. Moon, Regeneration of chronic rotator cuff tear in a rabbit model: synergistic benefits of human umbilical cord blood-derived mesenchymal stem cells, polydeoxyribonucleotides, and microcurrent therapy, *BioMed Res. Int.* 2022 (2022).
- [87] D. Rak Kwon, S. Jung, J. Jang, G.-Y. Park, Y. Suk Moon, S.C. Lee, A 3-dimensional bioprinted scaffold with human umbilical cord blood-mesenchymal stem cells improves regeneration of chronic full-thickness rotator cuff tear in a rabbit model, *Am. J. Sports Med.* 48 (4) (2020) 947–958.
- [88] D.R. Kwon, G.-Y. Park, S.C. Lee, Regenerative effects of mesenchymal stem cells by dosage in a chronic rotator cuff tendon tear in a rabbit model, *Regen. Med.* 14 (11) (2019) 1001–1012.
- [89] D.R. Kwon, Y.S. Moon, Synergic regenerative effects of polydeoxyribonucleotide and microcurrent on full-thickness rotator cuff healing in a rabbit model, *Ann. Phys. Rehabil. Med.* 63 (6) (2020) 474–482.
- [90] D.R. Kwon, G.-Y. Park, Y.S. Moon, S.C. Lee, Therapeutic effects of umbilical cord blood-derived mesenchymal stem cells combined with polydeoxyribonucleotides on full-thickness rotator cuff tendon tear in a rabbit model, *Cell Transplant* 27 (11) (2018) 1613–1622.
- [91] D.R. Kwon, G.-Y. Park, S.C. Lee, Treatment of full-thickness rotator cuff tendon tear using umbilical cord blood-derived mesenchymal stem cells and polydeoxyribonucleotides in a rabbit model, *Stem Cell. Int.* 2018 (2018).